New U-Th/Pb constraints on timing of shearing and long-term slip-rate on the Karakorum fault

Franck Valli,[1] Philippe Hervé Leloup,[2] Jean-Louis Paquette,[3] Nicolas Arnaud,[4] Haibing Li,[1,5] Paul Tapponnier,[1] Robin Lacassin,[1] Stéphane Guillot,[6] Dunyi Liu,[5] Etienne Deloule,[7] Zhiqin Xu,[5] and Gweltaz Mahéo[2]

[1] Zircons and monazites from 6 samples of the North Ayilari dextral shear zone (NAsz), part of the Karakorum fault zone (KFZ), have been dated with the U-Th-Pb method, using both ID-TIMS and SIMS techniques. The ages reveal (1) inheritance from several events spanning a long period between the late Archean and the Jurassic; (2) an Eocene-Oligocene magmatic event ($\sim35-32$ Ma); (3) an Oligo-Miocene magmatic event ($\sim25-22$ Ma), at least partly synkinematic to the right-lateral deformation; and (4) a period of metamorphism metasomatism ($\sim22-14$ Ma) interpreted as thermal and fluid advection in the shear zone. The Labhar Kangri granite located ~375 km farther Southeast along the KFZ is dated at 21.1 ± 0.3 Ma. Such occurrence of several Oligo-Miocene granites along the KFZ, some of which show evidence for synkinematic emplacement, suggests that the fault zone played an important role in the genesis and /or collection of crustal melts. We discuss several scenarios for the onset and propagation of the KFZ, and offset estimates based on the main sutures zones. Our preferred scenario is an Oligo-Miocene initiation of the fault close to the NA range, and propagation along most of its length prior to ~19 Ma. In its southern half, the averaged long-term fault-rate of the KFZ is greater than 8 to 10 mm/a, in good agreement with some shorter-term estimates based on the Indus river course, or Quaternary moraines and geodesy. Our results show the KFZ cannot be considered as a small transient fault but played a major role in the collision history. **Citation:** Valli, F., et al. (2008), New U-Th/Pb constraints on timing of shearing and long-term slip-rate on the Karakorum fault, *Tectonics*, *27*, TC5007, doi:10.1029/2007TC002184.

1. Introduction

[2] Whether strike-slip shear zones in continental collision domains are long-term lithospheric features, steadily accommodating large amounts of strain during long time spans, or short-lived and more transient features participating in distributed regional deformation of the crust remains a topic of debate. In the case of the India-Eurasia collision, interest focus on the main strike-slip faults bounding, or cutting across, the Tibetan plateau (inset Figure 1). Some consider that such faults play a major role in absorbing the convergence [e.g., *Tapponnier et al.*, 1986, 2001], while other think that they are negligible [e.g., *England and Houseman*, 1986].

[3] In northern and eastern Tibet, far from the Indus-Tsangpo suture zone and the Himalayas, large finite motions along major strike-slip faults are well documented. The sinistral Ailao Shan-Red River Shear Zone appears to have moved for 700 ± 200 km [*Leloup et al.*, 1995], since at least 33 Ma until ~17 Ma [*Briais et al.*, 1993; *Leloup et al.*, 2001; *Gilley et al.*, 2003]. Along the northern boundary of Tibet, the Altyn Tagh fault accrued ~375 km of sinistral offset since the Early Miocene at the longitude $\sim90°$E [*Ritts and Biffi*, 2000; *Yue et al.*, 2001; *Ritts et al.*, 2004]. More to the west, at $\sim83°$E, it offsets up to ~600 km a Permian batholith [e.g., *Tapponnier et al.*, 2001; *Ritts and Biffi*, 2000; *Yue et al.*, 2001; *Ritts et al.*, 2004]. These two faults are long-lasting boundaries allowing lateral motion of large portions of the continental lithosphere.

[4] In western Tibet, much closer to the Himalayas, it is still disputed if a major long-lasting strike-slip boundary developed and remained stable for several tens of millions of years in a context of thick and hot continental crust. To this respect, key points are the timing of initiation, the rate(s), the finite offsets, and the propagation history of the 1000-km long, active Karakorum Fault zone (KFZ). Proposed timing for the onset of the KFZ varies between less than 5 Ma ago to possibly more than 32 Ma [*Searle*, 1996; *Searle et al.*, 1998; *Phillips et al.*, 2004; *Searle and Phillips*, 2004, 2007; *Murphy et al.*, 2000; *Valli et al.*, 2007; *Lacassin et al.*, 2004a, 2004b; *Rolland et al.*, 2008].

[1]Equipe de tectonique, mécanique de la lithosphère, Institut de Physique du Globe de Paris, CNRS - Université Paris 7, Paris, France.

[2]Laboratoire des Sciences de la Terre, Université de Lyon, Ecole Normale Supérieure de Lyon, Université Claude Bernard Lyon 1, CNRS UMR, Villeurbanne, France.

[3]Laboratoire Magmas et Volcans, CNRS UMR, Université Blaise Pascal, Clermont-Ferrand, France.

[4]Géosciences Montpellier, Université Montpellier 2, CNRS UMR, Montpellier, France.

[5]Laboratory of Continental Dynamics, Institute of Geology, CAGS, Beijing, China.

[6]Laboratoire de Géologie des Chaînes Alpines, CNRS UMR, Université de Grenoble, Grenoble, France.

[7]Centre de Recherches Pétrographiques et Géochimiques, CNRS UPR, Nancy, France.

[5] Such age constraints are mostly derived from the study of ductile deformation along the KFZ in the Pangong area, as well as in the North Ayilari range (NA range) ~200 km further to the SE (Figure 1). Here, we present new U-Th-Pb ages obtained by Isotopic Dilution and Thermo Ionisation Mass Spectrometry (ID-TIMS) and Secondary Ion Mass Spectrometry (SIMS), on zircon and monazite grains from the NA range. Combined with structural evidence our ages bring constraints on the time relationships between magmatism, metamorphism and right-lateral deformation in the NA range and allow discussion on the long-term fault rates of the Karakorum fault zone.

2. Geological Setting of the North Ayilari (NA) Range

2.1. Karakorum Fault Zone

[6] The Karakorum fault zone (KFZ) is a major right-lateral active fault, stretching for more than 1000 km from the Pamir to the Indus-Tsangpo suture zone suture (Figure 1) [e.g., *Armijo et al.*, 1986, 1989; *Ratschbacher et al.*, 1994; *Chevalier et al.*, 2005; *Lacassin et al.*, 2004a].

[7] Near Gar, the North Ayilari active fault (NAaf) segment of the KFZ trends more northerly and has a normal component of slip, leading to the subsidence of the Gar pull-apart, and the uplift of the ~6000 m high North Ayilari (NA) range (Figures 1 and 2) [e.g., *Armijo et al.*, 1986, 1989; *Chevalier et al.*, 2005]. Such recent uplift induced the exhumation of granitoids and gneisses corresponding to a ~5 km wide shear zone parallel to the NAaf: the North Ayilari shear zone (NAsz). This shear zone corresponds to a deep portion of the KFZ [*Matte et al.*, 1996; *Lacassin et al.*, 2004a], continuously deformed, cooled and exhumed since ~21 Ma [*Valli et al.*, 2007] (Figure 2). Most samples of this study come from the NA range (Figure 2).

[8] Further to the SE, the KFZ prolongates along the Indus-Tsangpo suture zone eastward of the Kailas range (Figure 1). No other gneisses are found along the fault trace but dextrally sheared schist outcrop south of the Mt Kailas [*Lacassin et al.*, 2004a]. Farther East the active strand of the KFZ bounds the Labhar Kangri granite to the north (Figure 1). In order to discus the age of that granitoid and its relationship with shearing along the KFZ sample K2P30 was taken from its undeformed southern margin.

2.2. Ductile Deformation Linked With the Karakorum Fault Zone: The North Ayilari Shear Zone (NAsz)

[9] Ductile deformation in the NAsz is described by *Lacassin et al.* [2004a], and *Valli et al.* [2007, section 3, Figures 4, 5, and 6]. Along the NA range northeastern margin most rocks are mylonitized and show a steep high temperature (HT) foliation, striking almost parallel to the NAaf (Figure 2a). That foliation becomes flatter in the core of the range where deformation is milder (Figure 2). Close to the NAaf, the HT foliation is overprinted by a green schist foliation and by brittle-ductile deformation related to the active fault zone (Figure 2). The HT foliation bears a nearly horizontal stretching lineation, which is everywhere parallel to the NAaf even when foliation is flat (Figure 2). Deformation is unambiguously rotational, and shear senses are right-lateral where the foliation is steep (Figures 3c and 3d), and top to the southeast where the foliation is nearly horizontal (Figure 3b). Such geometry with flat foliation away from the core of the shear zone is observed in major strike-slip zones as the Ailao Shan Red River in SE Asia [e.g., *Leloup et al.*, 1995], and is consistent with an overall dextral ductile shearing in a ~5 km wide shear zone parallel to the NAaf: the North Ayilari shear zone (NAsz) [*Valli et al.*, 2007].

[10] From the study of quartz and feldspar microstructures, *Valli et al.* [2007] concluded that dextral shearing in the NAsz was continuous from 700–400°C to temperatures lower than 250°C. Unfortunately, in the absence of index minerals, particularly garnet, and due to the overprinting of early structures by lower temperature ones, the peak temperature reached during shearing cannot be precisely documented but is clearly above 400°C.

2.3. Relationships Between Magmatic and Mylonitic Rocks. Structural Setting of Dated Samples

[11] Locally, undeformed granites and leucocratic dykes crosscut the HT foliation. For example, in the southwest part of section 1, a large granite body intrudes migmatitic gneisses (Figure 1) that show top to the SE directed shearing parallel to the NAsz on flat-lying foliation. The migmatitic gneisses can be found as panels within the granite. Sample L89 corresponds to the leucosome of migmatitic gneisses outside of the granite (Figures 3a and 3b). Undeformed leucocratic veins cut across both the granite and the migmatitic gneisses (Figure 3h).

Figure 1. Structural map of western Tibet showing the Karakorum fault zone and adjacent units. Inset shows location in large-scale Asian active tectonic framework. Faults are mapped from *Brunel et al.* [1994], *Lacassin et al.* [2004a], *Ministry of Geology of USSR* [1989], *Tapponnier et al.* [2001], and *Weinberg and Dunlap* [2000]. The Oligo-Miocene magmatic intrusions are mapped from this study, *Dunlap et al.* [1998], *Lacassin et al.* [2004a], *Phillips et al.* [2004], *Searle* [1991], and *Searle et al.* [1992, 1998]. Contours for the ultrapotassic and potassic volcanism, together with North and High Himalayan granites are from [*Arnaud*, 1992; *Deng*, 1989; *Harrison et al.*, 1997, 1999; *Jiao et al.*, 1988; *Liu and Maimaiti*, 1989; *Miller et al.*, 1999]. PU, Plutonic Unit; GMDS, Gurla Mandhata detachement system; TSZ, Thanglasgo Shear Zone; SF Shigar fault; SKF South Karakorum fault; MBT Main boundary thrust; MMT main mantle thrust; MCT main central thrust; MKT main Karakorum thrust. Different grey levels highlight the main blocks and the ophiolitic sutures separating them. Map projection is UTM 44, ellipsoid WGS84.

[12] Closer to the NAaf, for example in the NE part of sections 2 and 3, such leucocratic veins are strongly sheared (Figure 3e) and interlayered with right-lateraly sheared, biotite-rich and two-mica mylonites (Figure 3g). P20 (K1P20 of *Lacassin et al.* [2004a, 2004b]) corresponds to such biotite rich (~40%) orthogneiss (Figure 2). P18, located ~300 m farther NE is a dextrally sheared two micas orthogneiss (Figures 2 and 3c). In a similar structural location, P34 (Figure 2) is a leucocratic mylonitic orthogneiss (Figure 3d) located in the NE part of section 2.
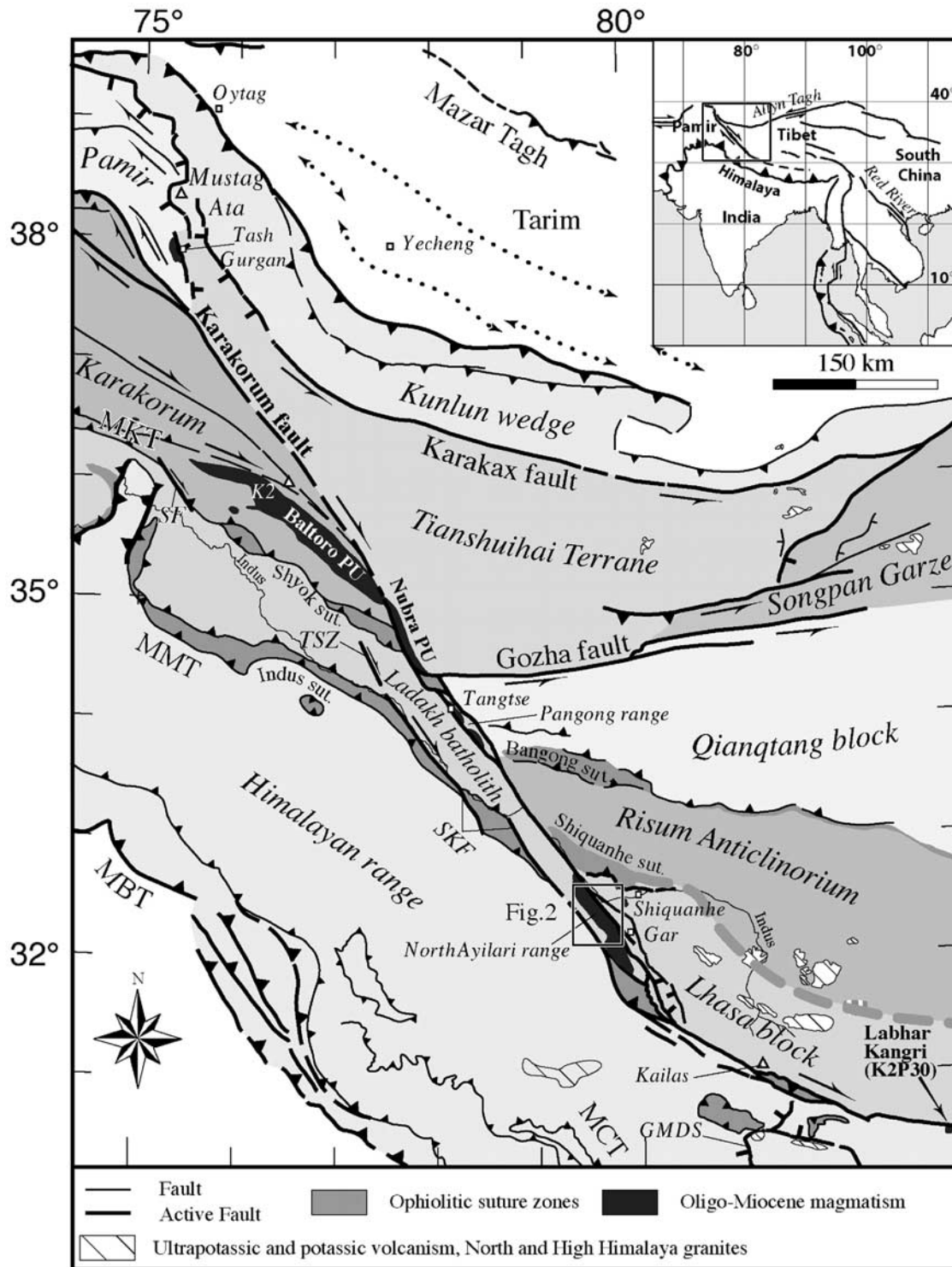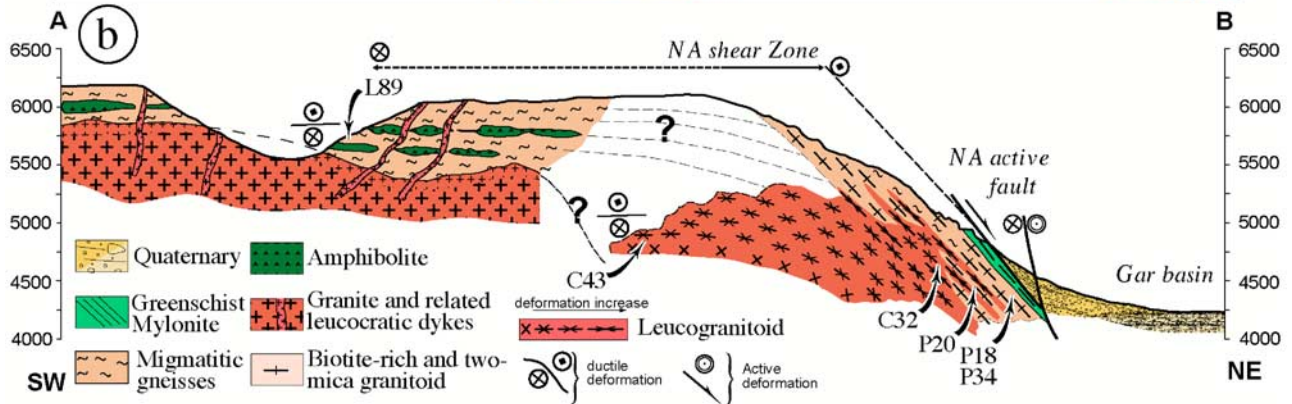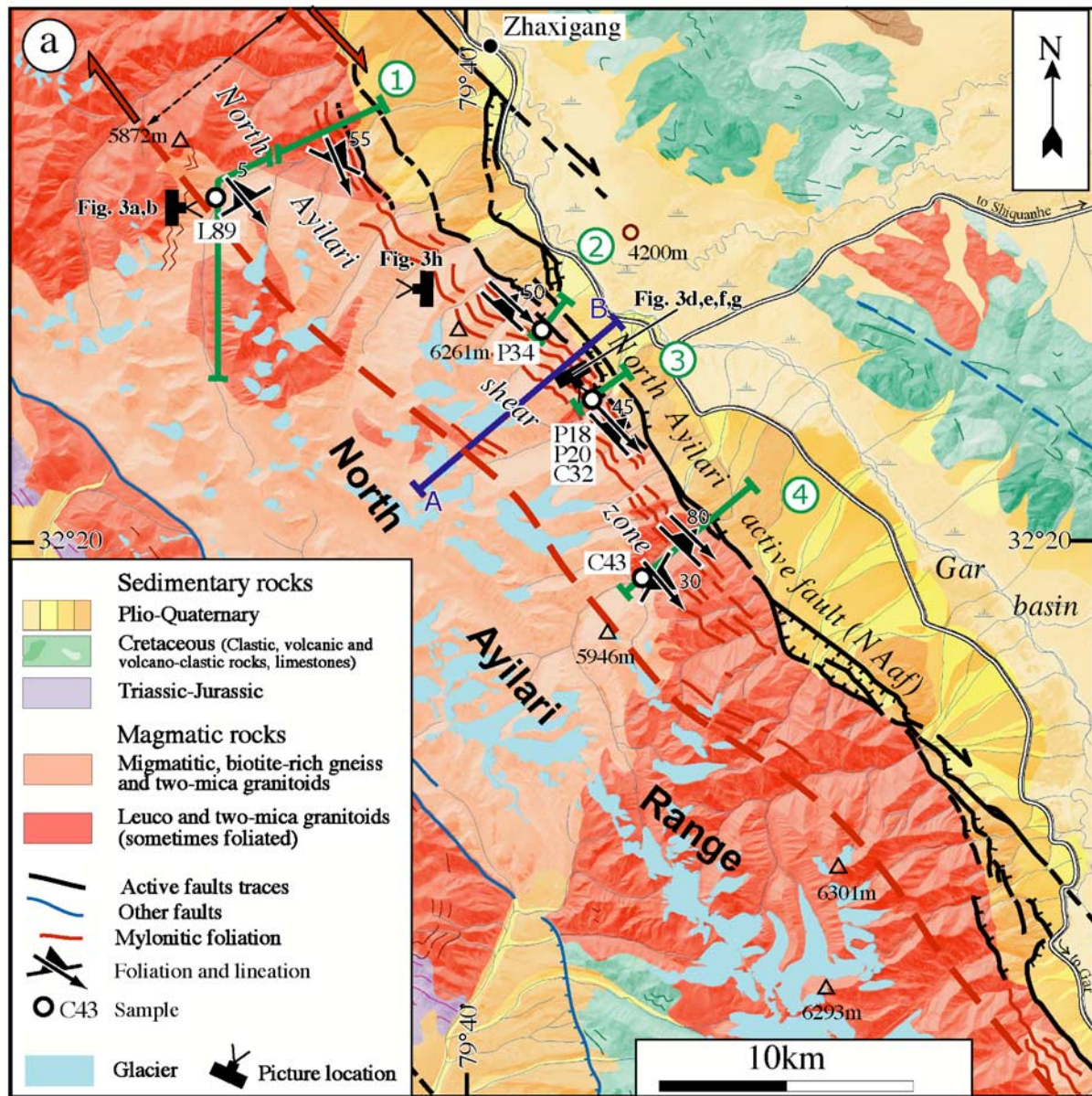

Figure 1

Figure 2

[13] Along section 3, the density of leucocratic veins increases toward the SW. Outcrop 3-A exhibits a large amount of leucocratic dykes, either deformed and transposed parallel to the foliation within the gneisses (T) or mildly to undeformed dykes (C) that crosscuts the foliation and the deformed dykes at high angle (Figure 3f). These field relationships indicate that the dykes are synkinematic to the right-lateral deformation. Sample C32 (K1C32 of *Lacassin et al.* [2004a, 2004b]) is a mildly deformed crosscutting dyke (Table 1, Figures 2 and 3f).

[14] Five kilometers to the SE, section 4 is exclusively made of sheared leucocratic orthogneisses with steep foliation in the NE that shallows to the SW (Figure 2). C43 leucocratic orthogneiss, was sampled where foliations are flatter and deformation mild (Figure 2) but shows top to the southeast shear sense.

[15] The field relationships described above can be summarized as follows. (1) The migmatitic gneisses (L89) are sheared within the NAsz but are intruded by the granite outcropping in section 1. (2) The leucocratic dykes (C32) intrude all units, including the granite and the dextrally sheared rocks (P18, P34), but (3) close to the NAaf they are all strongly sheared and transposed parallel to the right-lateral HT foliation and appear synkinematic to the right-lateral ductile deformation [*Valli et al.*, 2007].

3. Geochronology Analytical Methods

[16] Zircon and monazite grains were separated using a Wilfley table, heavy liquids and a Frantz magnetic barrier separator. The final selection of grains according to color and morphology was done using a binocular microscope. The fractions selected for ID-TIMS dating (C43 monazite, C32 zircon and monazite, and P30 zircon) were washed in hot 4 M HNO_3 and H_2O respectively. The selected grains were dissolved using 29 M HF for zircons or 8 M HCl for monazites in PFA Teflon Ludwig-type Savillex microcapsules [*Parrish*, 1987] at 220°C, during 24 h (monazite) to 60 h (zircon). Chemical separation and mass spectrometry were performed according to *Paquette and Pin* [2001]. The U and Pb isotopes were measured on a VG Sector 54W mass spectrometer in multicollector static mode. The isotopic ratios are corrected for mass discrimination (0.1 ± 0.015% per amu for Pb and U), isotopic tracer contribution and analytical blanks: 7 ± 2.5 pg for Pb and less than 1 pg for U. Initial common Pb is corrected for each fraction using

the *Stacey and Kramers* [1975] two-step model. Data errors (2σ) of the zircon fractions and ages were calculated using the PBDAT 1.24 and Isoplot/Ex 3.23 programs [*Ludwig*, 1993, 2003].

[17] For in situ ion microprobe analyses, the selected grains were mounted together with standard in epoxy resin. The mounts were then abraded and polished to expose at the surface the middle part of the crystals. Each grain was imaged using cathodoluminescence (CL) and backscattered electron (BSE) scanning microscope to characterize the zoning patterns and inner structures. In situ dating of monazite was also performed from rock thin sections, which allows preserving the potential links between the measured ages and the textural location of the grains. Using a diamond saw specific zones from the thin sections containing the radiogenic minerals were extracted. Pieces were then mounted together with zircon and/or monazite standard in epoxy resin and then polished. MOACIR monazite standard [*Seydoux-Guillaume et al.*, 2002] and 91500 zircon standard [*Wiedenbeck et al.*, 1995] were used for samples P20, and TEMORA 1 for all the others [*Black et al.*, 2003]. Zircons in samples P18, P34, C43, L89 and monazites in sample L89 were analyzed for U, Th and Pb isotopes using the sensitive high resolution ion microprobes (SHRIMP II) at the Institute of Geology of Beijing, China, while zircons in sample P20 and monazites in sample P18 were measured using the Cameca IMS 1270 at CRPG in Nancy, France. Calibration parameters, data acquisition and age correction are described by *Compston et al.* [1984] for the SHRIMP II, and by *Deloule et al.* [2001] for the Cameca IMS 1270. The error on the calibration curve is taken into account for the age uncertainty calculation. The spot size was between 30 and 60 μm, and their contours were precisely drawn after each analytical session using secondary and backscattered electron (BSE) images.

[18] Ion probe U-Th-Pb dating of young minerals is an analytical challenge because of the very small amounts of radiogenic daughter isotopes (^{206}Pb, ^{207}Pb, ^{208}Pb). In case of recent minerals, it is now usual for most geochronologists to consider the ^{238}U/^{206}Pb ages as the most reliable for zircons [e.g., *Stern and Amelin*, 2003], and the ^{232}Th/^{208}Pb ages for monazites [e.g., *Catlos et al.*, 2004]. The isotopic systems of zircons and, to a lesser extent, monazites keep the memory of several distinct magmatic, metamorphic and hydrothermal events. This provides the opportunity to reconstruct complex geological histories but requires cau-

Figure 2. Geology of the North Ayilari range and samples location. (a) Geological map of the North Ayilari (NA) range between Zhaxigang and Gar. Drawn from field observations along the four cross-sections depicted in green (see detailed sections in Figure 4 of *Valli et al.* [2007]), and satellite image interpretation (Landsat 7, Spot 5, and SRTM DEM). Light shading outlines topography. Section A-B corresponds to Figure 2b. Numbers near foliations symbols give the foliation dip. South West boundary of the North Ayilari dextral shear zone is crudely depicted by a dashed red line. Projection is UTM 44, ellipsoid WGS84. Figure 3 pictures are located. (b) Generalized cross-section of North Ayilari (NA) range northeastern flank, across the North Ayilari shear zone (NAsz) and active fault (NAaf). Drawn from extrapolation between field observations along cross sections shown in Figure 2a. U-Th/Pb samples are located with black arrows. Note that because magmatic rocks mapping Figure 2a is mostly based on reflectance properties while section Figure 2b is draw from direct field observations, the map is less detailed and the two legends differ.
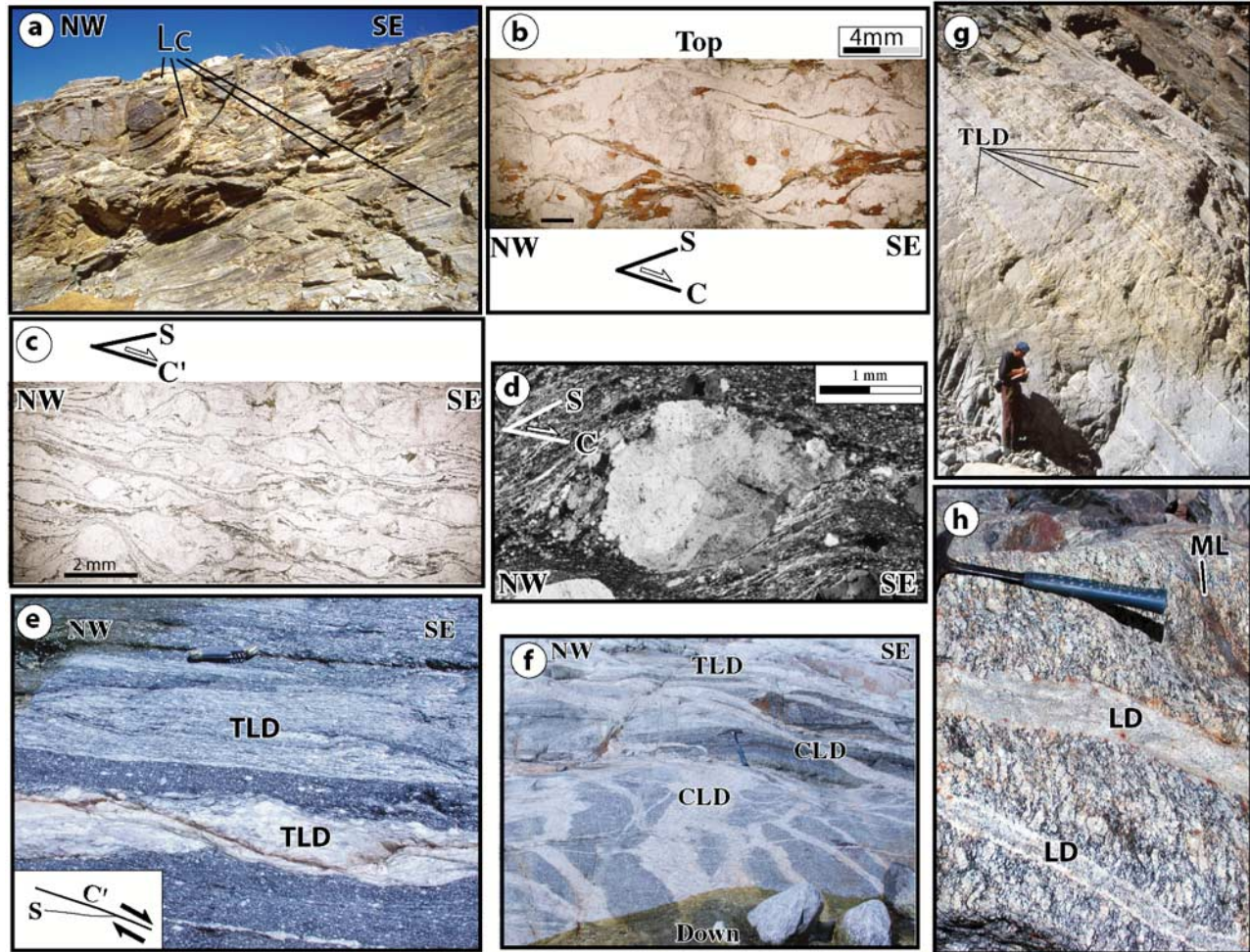
Figure 3. North Ayilari range pictures showing structural relationships between magmatic and metamorphic rocks. (a) Flat lying migmatitic gneisses, section 1, see Figure 2. Lc: leucosome. The gneisses exhibit a N 140 trending lineation and top to the SE shear criteria (see Figure 3b). (Figures 3b–3d) Rock thin sections perpendicular to foliation and parallel to lineation. (b) C/S structures in migmatitic gneisses (see Figure 3a) indicating top to the SE shearing. Sample L89 (Figure 2). (Figure 3c) Dextral shear planes. Sample P18, section 3 (Figure 2). (Figure 3d) σ-type feldspar mantled by dynamically recrystallized grains in low stress areas; asymmetry indicates dextral shear sense (sample P34, section 2, Figure 2). (e–g) Variously deformed generations of syn-kinematic leucocratic dykes intruding the Kfz HT foliation. (e) Highly deformed leucocratic dykes (TLD) transposed parallel to the surrounding N140 trending HT foliation of the NAsz. Knife gives scale. (f) Outcrop 3A, section 3, see Figure 2 for location. TLD: transposed and highly deformed veins (see Figure 3e), CLD: less deformed crosscutting veins (sample C32). Hammer gives scale, view from SW. (g) Leucocratic dykes transposed parallel to the NAsz HT foliation (TLD). Section 3, see Figure 2 for location. (h) undeformed leucocratic dyke (LD) crosscutting migmatitic gneisses. ML: melanosome. Hammer gives scale. Boulder falling from the flanks of a valley between section 1 and 2, see Figure 2a for location.

tious interpretation of the analytical results to individualize the different populations.

[19] Within a given population of ion probe data, it is important to distinguish meaningful ages from outliers, which can always occur in spite of careful selection of rocks and minerals, and of rigorous analytical conditions. Age disparity around a mean value may results either from (1) an overlap of the probe beam on zones of distinct ages,

(2) large SIMS analytical errors related to low radiogenic Pb content in young zircon overgrowths [*Stern*, 1997], (3) the occurrence of common Pb, (4) ^{230}Th radioactive disequilibrium in monazites [*Schärer*, 1984], (5) a partial lead loss due to (a) subsequent high temperature event(s), (6) a combination of these points. For example, zircon z227 of sample C43 gives significantly distinct ages at its two tips that should a priori give similar ages because they belong to

Table 1. Location (see Also Figure 1 and 2) and Description of Dated Samples[a]

Sample	Range/Section	Latitude, ° ' ".	Longitude, ° ' ".	Altitude, m	Facies	Structure	Zr U/Pb Results	Mz U/Pb Results
L89	North Ayilari / section 1	N32°26'44.63"	E79°33'36.55"	5046	migmatitic leucosome	Fo: N60, 5N; Li az 140	Figure 5, Table 2	Figure 6, Table 3
P34	North Ayilari / section 2	N32°25'00.40"	E79°42'06.10"	4573	leucocratic mylonitic gneiss	Fo: N134, 37N; Li az 134	Figure 8, Table 6	
P18	North Ayilari / section 3	N32°23'28.90"	E79°43'35.00"	4501	two micas orthogneiss	Fo: N140, 50N; Li az 139	Figure 9, Table 7	Figure 11, Table 8
P20	North Ayilari / section 3	N32°23'19.20"	E79°43'27.70"	4633	biotite-rich gneiss	Fo: N145 37N; Li az 139	Figure 12, Table 9	
C32	North Ayilari / section 3	N32°23'17.60"	E79°43'25.30"	4637	leucocratic dyke	mild deformation, crosscuts NW–SE foliation	Figure 13, Table 5	Figure 13, Table 5
C43	North Ayilari / section 4	N32°19'22.70"	E79°44'25.30"	4797	leucocratic orthogneiss	Little deformation, C/S structures	Figure 7, Table 4	Table 5
K2P30	Labhar Kangri	N30°28'59.20"	E83°02'22.30"	5451	granite	no deformation	Figure 14, Table 10	

[a]Fo: foliation, Li: lineation, az: azimuth, Mz: monazite, Zr: zircon.

the same growing band (z227-2 & -3, Table 4 and Figure 4b). One of these two ages is among the youngest of its population while the other is the oldest. It is very difficult to determine which result is the most significant. Consequently, we consider that the best age estimate of a given population of ion probe data is its mathematical mean with a two standard deviation uncertainty, which will lower the influence of outlier(s).

4. U-Th-Pb Data and Interpretations

[20] The Tertiary SIMS data are plotted on the Tera-Wasserburg diagram [*Tera and Wasserburg*, 1972] (1σ error crosses for readability) while others data are plotted in concordia diagrams (2σ ellipse errors or larger symbols when ellipses are too small). Errors mentioned in the text are at the 2σ level, the weighted averages, and the associate 95% confidence errors, were calculated with Isoplot 3.23 of *Ludwig* [2003].

4.1. Top to the South Sheared Rocks in the Core of the NA Range

4.1.1. Migmatitic Leucosome L89
4.1.1.1. Zircons
[21] Sixteen zircons were imaged and in situ dated using SHRIMP II (Table 2). The zircon grains are euhedral to subhedral and exhibit distinct rim-core domains and oscillatory zoning (e.g., Figure 4).

[22] Zircon z28 is euhedral and exhibits an oscillatory zoning pattern (Figure 4a). The crystal core is characterized by a magmatic Th/U ratio and yields a 34.7 ± 2.4 Ma $^{206}Pb/^{238}U$ age (Table 2). A small euhedral zircon grain (z34) also displaying a magmatic Th/U ratio is dated at 23.4 ± 4.0 Ma. Twelve grains are concordant and have inherited $^{206}Pb/^{238}U$ ages between 200 and 500 Ma, possibly representing several Triassic to Cambrian magmatic events or a rough discordia trajectory between 23–35 Ma intercepts and ∼500–600 Ma (Figure 5). Two other analyzed grains (z29, z33) are significantly discordant indicating Proterozoic to Archean $^{207}Pb/^{206}Pb$ ages of 1.7 and 2.6 Ga. Owing to the very small size of the zircon grains, the probe beam often crosscut cores and overgrowth domains, implying that some ages may correspond to mixed values.

4.1.1.2. Monazites
[23] Eleven subhedral to anhedral monazites coming from sample L89 were dated in thin section with the SHRIMP II. One grain (M1) shows Mesozoic inheritance (Table 3). The ten remaining monazite grains yield $^{208}Pb/^{232}Th$ ages ranging from 25.4 ± 3.6 Ma to 13.1 ± 5.1 Ma (Figure 6). Note that the oldest monazites, found in inclusions within biotites and chlorites (M3-1, 2 and M25), have an average age broadly synchronous with magmatic zircon z34 suggesting crystallization of the rock at ∼24.2 ± 2.4 Ma (Figure 6). Younger ages can be related to several crystallization events between ∼22–13 Ma, or to partial opening of the Th-Pb system at ≤13 Ma.

4.1.2. C43 Leucocratic Orthogneiss
[24] Eleven zircon grains were selected for ID-TIMS and SHRIMP II dating. Zircon rims are dark in CL images
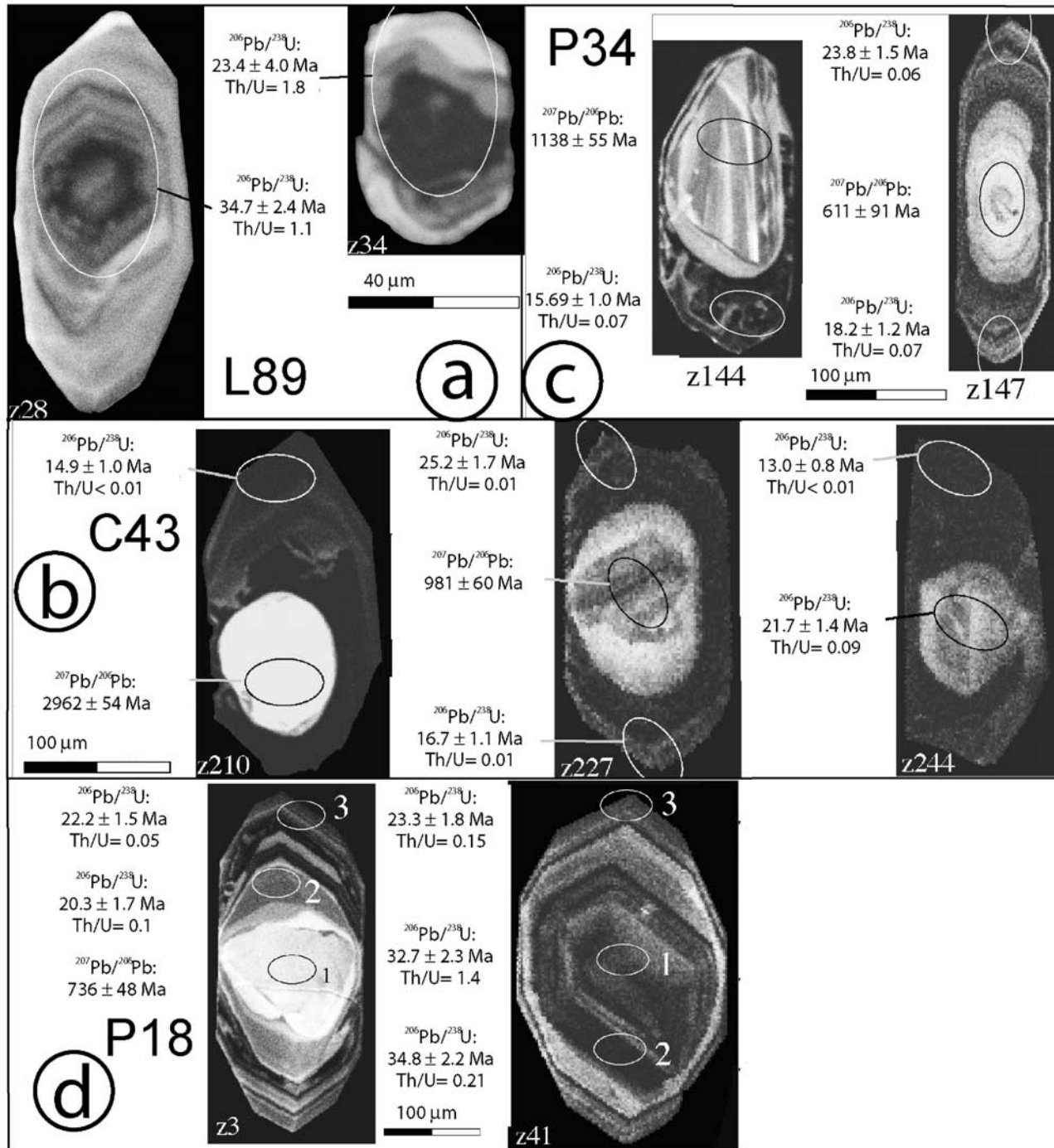
Figure 4. Examples of CL images of dated zircons. Ellipses show ion probe spots with corresponding $^{206}Pb/^{238}U$ or $^{207}Pb/^{206}Pb$ ages and Th/U ratio. (a) Tertiary zircons from migmatitic gneiss L89 (section 1, Figures 2, 3a, and 3b, and Table 2). (b) zircons from C43 leucocratic orthogneiss (section 4, Figure 2, and Table 4). (c) mylonitic leucocratic gneiss P34 (section 2, Figure 2, and Table 6). (d) two-mica orthogneiss P18. Zircon grain Z3 exhibits a core surrounded by a darker rim while Zircon grain Z41 shows uniform oscillatory zoning without any clear rim-core domains (Table 7).

Table 2. Migmatitic Gneiss L89 Zircon SHRIMP II Data[a]

Spot Name	Age, Ma 206/238	±(2σ)	Age, Ma 207/235	±(2σ)	Age, Ma 207/206	±(2σ)	CL Domain	206/238	±%	207/235	±%	U, ppm	Th, ppm	Th/U	Type	206Pb[a], ppm	% com Pb
z34	23.4	4.0	-	-	n.s.		n.d.	0.00363	17.4	-	-	1579	2497	1.75	Ma	9.6	52.7
z28	34.7	2.4	33.1	18.8	n.s.		OC	0.00539	6.8	0.0331	58	3041	3305	1.12	Ma	16	15.1
z29	82.3	6.2	173	62	1711	690	n.d.	0.01284	7.6	0.1855	39.2	1126	55	0.05	Ma-Me	15	25.5
z52	204	12	240	29	606	260	n.d.	0.03216	5.8	0.2664	13.6	2175	43	0.02	Ma-Me	63	4.7
z27	333	20	342.1	64.6	404	470	n.d.	0.05301	6.2	0.4006	22.2	615	25	0.04	Ma-Me	29	3.1
z36	342	21	351	56	408	390	n.d.	0.05452	6.4	0.4127	19	874	24	0.03	Ma-Me	43	4.5
z40	349	20	340	30	n.s.		n.d.	0.05557	6	0.3973	10.6	636	279	0.45	Ma	31	3.2
z41	393	24	365	132	517	330	n.d.	0.06289	6.4	0.4319	43	483	242	0.52	Ma	29	12.6
z30-2	395	23	413	55	n.s.		n.d.	0.06319	5.8	0.5023	16.2	1140	79	0.07	Ma-Me	65	4.5
z39-1	443	27	408	51	n.s.		n.d.	0.07118	6.2	0.494	15.2	897	44	0.05	Ma-Me	57	2.6
z39-2	446	25	410	32	n.s.		n.d.	0.07159	5.8	0.4968	9.6	876	32	0.04	Ma-Me	54	0.2
z38	452	36	548	128	970	580	C	0.07258	8.2	0.715	30.2	560	56	0.1	Ma-Me	40	14.3
z30-1	474	28	450	79	n.s.		n.d.	0.07633	6	0.5579	21.6	982	55	0.06	Ma-Me	69	6.9
z51	498	28	529	45	667	200	n.d.	0.08023	5.8	0.6835	11	1851	142	0.08	Ma-Me	132	3.7
z26	500	32	440	131.1	n.s.		n.d.	0.08059	6.6	0.5429	36.6	1122	187	0.17	Ma	90	14.1
z42	535	30	642	114	1038	460	n.d.	0.08655	5.8	0.8815	23.8	733	224	0.32	Ma	55	5.8
z33	1463	83	2006	59	2624	40	n.d.	0.25476	6.4	6.2121	6.8	635	122	0.2	Ma	140	1.2

[a]Results are presented by increasing $^{206}Pb/^{238}U$ ages. CL domains (within brackets when unclear): C, core; R, Rim; O oscillatory; n.d. not defined. Type, type of event on which the analyzed domain will provide an age constrain, Ma, magmatic; Me, Metamorphic. Th, and U concentration calculated following *Stern* [1997]. n.s., not significant.

indicating a higher U-content relative to their rounded or prismatic cores (Figure 4b). Ten zircon rims yield concordant ages ranging from 25.2 ± 1.7 Ma to 13.0 ± 0.8 Ma with a median value for the $^{206}Pb/^{238}U$ ages of $17.8 + 4.4/ -3.4$ Ma (Table 4 and Figure 7a). The Th/U ratios are systematically low (0.01–0.05), pointing out for strong Th depletion relatively to U, which is often related to the (re)-crystallization of the rims during metamorphism or metasomatism [*Rubatto et al.*, 2001]. These rims are strongly U-enriched (6800–20,000 ppm), compared to the cores. This implies that the crystallization of the rims happened in equilibrium with a fluid enriched in trace elements and especially in U [e.g., *Rubatto and Gebauer*, 1998]. This very high U concentration could have favored Pb-loss, producing the discordance of the analytical points along a chord close to the Concordia. However, this possibility is ruled out by the lack of any correlation between discordance level and U content, the rim growth is therefore most probably related to several hydrothermal pulses between ∼25 and ∼13 Ma. In addition, two monazite fractions analyzed by ID-TIMS are concordant at 14.4 ± 0.7 Ma (Table 5), implying the (re)crystallization of monazites at that time.

[25] Among eleven spots on zircon cores, a single one (z244-1) yields a subconcordant age of ∼22 Ma (Figure 7a) coinciding with zircon rims and displays intermediate Th/U ratio (0.09) and U-content (1379 ppm). All the other cores yield older ages ranging from $^{206}Pb/^{238}U$ ∼170 Ma to $^{207}Pb/^{206}Pb$ ∼3.0 Ga (Figure 7b). Most of these cores show high Th/U ratios (0.18–2.2) suggesting a magmatic origin (Table 5), but the analytical points are mostly discordant and it is impossible to distinguish a simple age pattern or to draw a significant discordia array (Figure 7b).

4.2. Right-Laterally Sheared Gneisses in the Core of the North Ayilari Shear Zone

4.2.1. P34 Leucocratic Mylonitic Orthogneiss

[26] Nine euhedral to subhedral grains (e.g., Figure 4c) were selected for in situ SHRIMP II dating. Most of the cores and rims exhibit oscillatory zoning, which are often disrupted in the complex and recrystallized cores.

[27] Five zircon rims characterized by low metamorphic Th/U ratio (0.01–0.08) yield concordant and nearly concordant tertiary $^{206}Pb/^{238}U$ ages ranging from 26.9 ± 1.6 to 18.2 ± 1.2 Ma with a mean of 22.1 ± 4.7 Ma (Table 6, and Figure 8a). U contents are higher in the rims (1400–2500 ppm) than in the cores (170–1300 ppm). This suggests rim formation by (re)crystallization in equilibrium with a metamorphic fluid enriched in trace elements [*Hoskin and Schaltegger*, 2003; *Rubatto and Gebauer*, 1998]. One core (z120-1, not plotted in Figure 8 since no reliable $^{207}Pb/^{235}U$ age was obtained), characterized by low metamorphic Th/U ratio (0.01), and low U-content (230 ppm), and by the absence of oscillatory zoning, yielded a 20.9 ± 2.2 Ma $^{206}Pb/^{238}U$ age. Three cores (z147-1, z156-1, z153-1) and one rim (z145-1, 3) yielded concordant ages around 300 Ma (Figure 8b and Table 6). The five other analyzed cores are
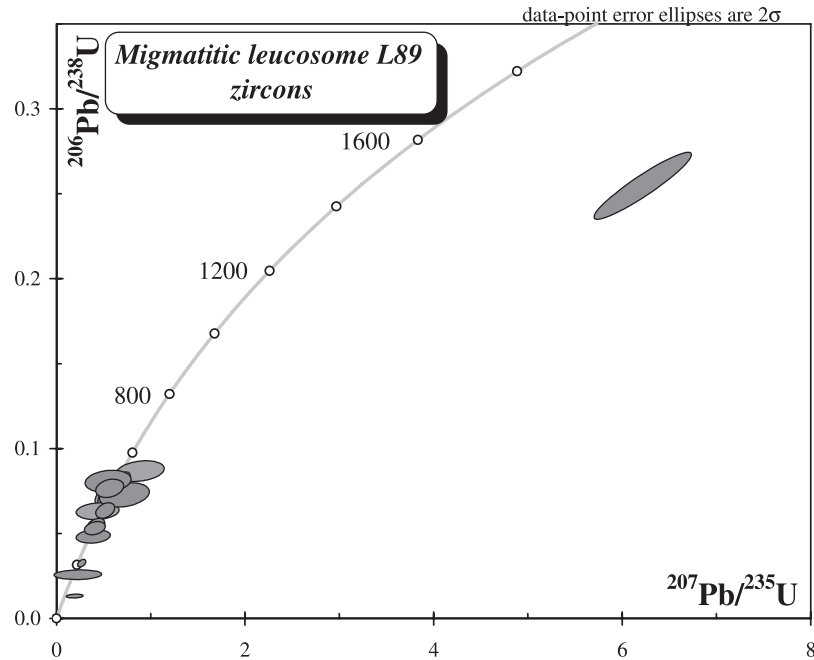
Figure 5. $^{206}Pb/^{238}U$ versus $^{207}Pb/^{235}U$ Concordia diagram of SHRIMP II in situ zircons ages of L89 migmatitic leucosome (section 1, Figures 2, 3a, and 3b).

significantly discordant and indicate Proterozoic $^{207}Pb/^{206}Pb$ ages between 0.9 Ga and 1.8 Ga.

4.2.2. P18 Two-Mica Orthogneiss

4.2.2.1. Zircons

[28] Twenty-four ages where obtained from ten zircon crystals using the SHRIMP II (Table 7). All zircons are euhedral, colorless, nonfractured, and contain rounded to prismatic cores. On CL images, eight of these crystals show rims much darker than cores (e.g., Figure 4d) indicative of higher U-content at their borders [*Hanchar and Rudnick*, 1995; *Rubatto and Gebauer*, 1998]. Some cores or rims exhibit clear oscillatory zoning. Only two zircons crystals (z8 & z41) present uniform oscillatory zoning patterns over the whole grain without any rim-core transition (Figure 4d).

Table 3. Migmatitic Gneiss L89 Monazite SHRIMP II Data, Results are Presented by Ascending $^{206}Pb/^{238}U$ ages

Spot Name	Age, Ma 208/232	±(2σ)	208/ 232	±%	Th, %	U, ppm	Th/U	208Pb[a], ppm	% com 208Pb	Structural Location
m29-2	13.1	5.1	0.000650	39.0	10.2	1395	72.9	32	7.3	Ic Bt
m38-2	14.9	3.6	0.000736	24.4	7.3	3071	23.8	10	22.8	Ic Bt
m2	15.3	4.2	0.000759	27.6	4.9	6942	7.0	21	29.5	It
m24	16.5	3.6	0.000818	22.0	5.9	7859	7.5	30	26.7	It
m32	16.7	7.2	0.000828	43.4	4.7	5010	9.4	10	58.8	It
m38-1	17.8	2.7	0.000882	15.0	4.7	2307	20.5	28	7.7	Ic Bt
m18	17.9	3.7	0.000888	20.6	5	3128	16.1	23	21.1	Ic Chl
m33-1	19.3	2.2	0.000956	11.4	5.9	4569	13.0	45	4.9	It
m29-1	19.4	4.8	0.000959	24.8	9.3	957	97.1	26	10.8	Ic Bt
m33-2	21.8	2.6	0.001081	11.8	7.2	8687	8.3	59	11.4	It
m25	23.1	6.9	0.001144	30.0	4.6	5713	8.1	21	51.1	Ic Chl
m3-2	23.3	3.7	0.001152	16.0	6.7	5836	11.5	46	18.2	Ic Bt
m3-1	25.4	3.6	0.001255	14.4	5.7	3638	15.6	52	8.0	Ic Bt
m1-2	152	14	0.007545	9.4	6.5	3835	17.0	319	10.0	Ic Bt
m1-1	248	11	0.012370	4.4	4.8	5846	8.2	478	6.4	Ic Bt

Structural location refers to the shape and position of the monazite crystal with respect to the surrounding minerals (Figure 10): It, interstitial; Ic, included, and the following abbreviation indicates the mineral in which the monazite is included. Bt., biotite; fs., Feldspar; Chl, Chlorite. Th and U concentrations are calculated following *Stern and Sanborn* [1998].

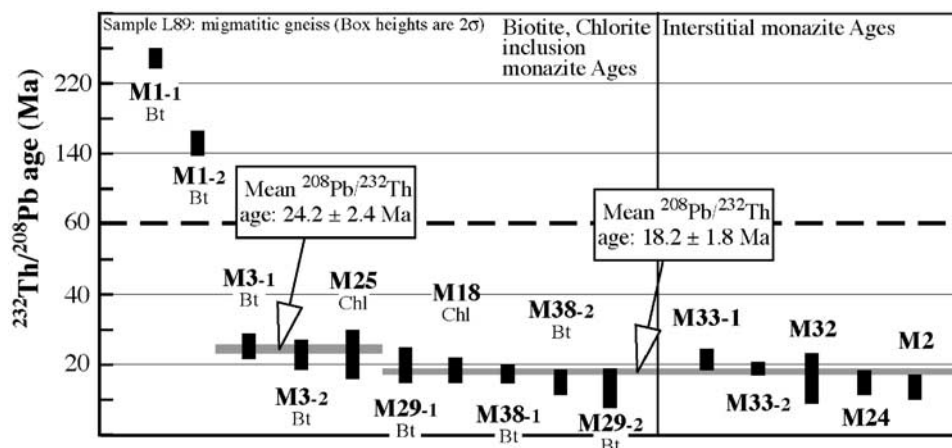[a]Represent the radiogenic component.

Figure 6. $^{208}Pb/^{232}Th$ ages from in situ IMS 1270 microprobe dating of L89 migmatitic gneiss monazite grains (section 1, Figures 2, 3a, and 3b). Each bar shows result and uncertainty for one grain, and ages are grouped according to their structural position. The mineral phases in which monazites are included are specified. Bt., Biotite; fs, Feldspar; Chl, Chlorite. Errors are given at 2σ. Light gray rectangles represent the preferred mean ages for interstitial and included monazite populations (see text for details). Note that the vertical scale changes above 60 Ma.

The $^{206}Pb/^{238}U$ ages measured in the central parts of these two grains are similar and yield a mean value of 34.4 ± 1.3 Ma (Table 7 and Figure 9a). Their Th/U ratios (0.21 to 1.40) rather favor a magmatic origin for the zircons [*Rubatto and Gebauer*, 1998]) as well as their continuous oscillatory-zoning patterns [*Gebauer*, 1996; *Rubatto and Gebauer*, 1998; *Schärer et al.*, 1995; *Vavra et al.*, 1996]. This suggests that magmatic zircons crystallized around 34 Ma are present in sample P18.

[29] Twelve analyses of the rims were performed, all ages being concordant or subconcordant within 2σ error limits, with $^{206}Pb/^{238}U$ ages spanning between 27.4 ± 1.9 and 19.8 ± 1.4 Ma (Table 7 and Figure 9a) with a $^{206}Pb/^{238}U$ median age of $23.3 + 4.0/-2.2$ Ma.

[30] Six zircon cores yield concordant $^{206}Pb/^{238}U$ ages spreading between 181 ± 13 and 438 ± 27 Ma (Table 7). Such ages could correspond either to several Lower Jurassic to Cambro-Ordovician magmatic events, or to a discordia line between $\sim34-23$ Ma and ~500 Ma intercepts (Figure 9b). Two cores give older $^{207}Pb/^{206}Pb$ apparent ages at ~1.0 and ~1.8 Ga, suggesting inheritance from Protero-zoic magmas.

4.2.2.2. Monazites

[31] Sixteen subhedral to anhedral monazites were dated in situ within thin sections (Table 8) using the SHRIMP II. On BSE images the grains display concentric to patchy zoning patterns (Figure 10). $^{208}Pb/^{232}Th$ apparent ages span between 27.9 ± 3.6 Ma and 13.5 ± 1.7 Ma with a relationship between the ages and the textural position of the grains (Figure 11 and Table 8). The four oldest mon-azites are included in biotite or feldspar crystals, with a mean $^{208}Pb/^{232}Th$ age of 25.2 ± 1.6 Ma, whereas the twelve remaining interstitial monazite grains display ages ranging from 23.7 ± 3.0 Ma to 13.5 ± 1.7 Ma with a mean of 18.8 ± 2.8 Ma.

[32] Included monazites are broadly synchronous with zircon magmatic rims which favor the hypothesis of the crystallization of the rock at $\sim25-23$ Ma. Th-Pb ages of interstitial monazites are younger, down to 13.5 ± 1.7 Ma (Figure 11). This could be related to the occurrence of one or several thermal pulses between ~23 and 13 Ma, as interstitial monazites are potentially more sensitive to hy-drothermal fluids than the included grains. The Th/Pb dating providing only apparent ages, this $25-13$ Ma spread in age could also be related to the discordancy of the analyzed spots toward a lower intercept at ≤13 Ma.

4.2.3. P20 Biotite-Rich Gneiss

[33] Four zircon grains were dated in thin sections with the Cameca IMS 1270. $^{206}Pb/^{238}U$ ages range between 23.9 ± 6.9 Ma and 19.9 ± 1.6 Ma with an average value of 21.7 ± 3.6 Ma (Table 9 and Figure 12). The high Th/U ratios suggest crystallization or recrystallization of magmatic zircon grains at ~22 Ma.

4.3. C32 Leucocratic Dyke

[34] Five zircon fractions were selected for ID-TIMS dating. The most acicular zircon grains (z1) yield a concor-dant age of 22.7 ± 0.1 Ma, while the four other fractions are discordant, and define a chord yielding a lower intercept at 32.5 ± 2.6 Ma and an upper intercept at 1296 ± 120 Ma (Figure 13 and Table 5).

[35] The concordant fraction at ~23 Ma most likely represents the crystallization of zircons during a high temperature event. The lower intercept at ~33 Ma may represent either a high temperature event, or may be related to a fortuitous alignment of inherited zircon grains affected by multiepisodic Pb loss. The good alignment and the position of the analytical points close to the lower intercept rather favor the first hypothesis. The syn-kinematic leucog-ranite C32 crystallized at ~23 Ma and probably represents
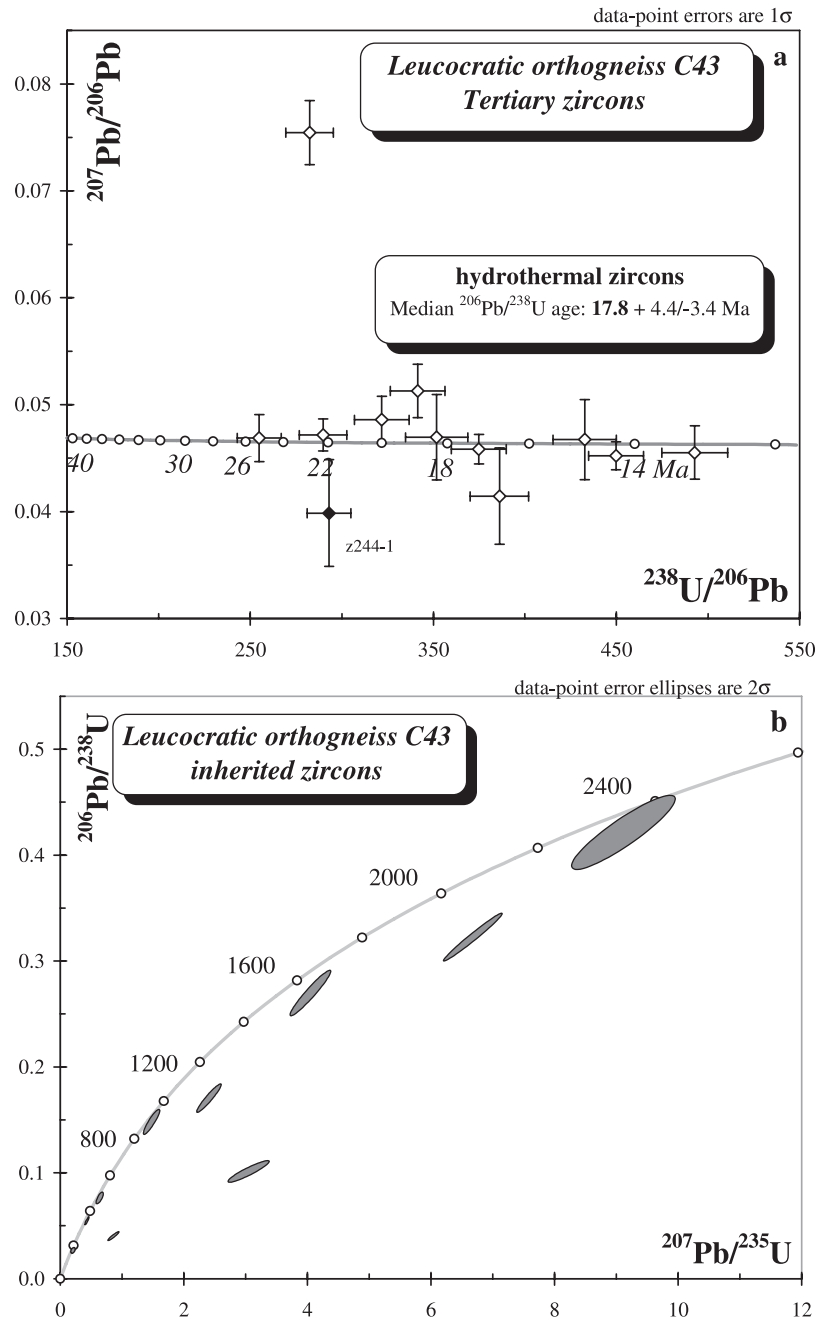
Figure 7. U-Pb SHRIMP II ages of zircons from C43 leucocratic orthogneiss (section 4, Figure 2). (a) Tertiary ages plotted in a Tera-Wasserburg diagram; white and black diamonds correspond to hydrothermal zircon rims and core, respectively. (b) Magmatic zircon core ages plotted in a ^{206}Pb/^{238}U versus ^{207}Pb/^{235}U Concordia diagram (Table 4).

Table 4. Sample C43 Sheared two-Mica Leucogranitoid Zircons SHRIMP II Data[a]

Spot Name	Age, Ma 206/238	±(2σ)	Age, Ma 207/235	±(2σ)	Age, Ma 207/206	±(2σ)	CL Domain	206/238	±%	207/235	±%	U, ppm	Th, ppm	Th/U	Type	206Pb[a], ppm	% com Pb
z244-2	13.0	0.8	11.7	2.0	n.s.		R	0.00202	5.8	0.0116	10.4	6795	15	<0.01	Hy	12	0.3
z240	14.3	0.8	13.6	1.1	n.s.		R	0.00222	5.7	0.0135	7.4	18,440	335	0.02	Hy	35	0.4
z210-2	14.9	1.0	15.0	2.5	n.s.		(OR)	0.00231	6.6	0.0149	16.6	7392	17	<0.01	Hy	15	1.4
z227-3	16.7	1.1	14.9	3.1	n.s.		(OR)	0.00259	6.7	0.0148	21.2	8724	67	0.01	Hy	20	0.8
z219-1	17.2	1.1	17.0	1.3	n.s.		R	0.00267	6.4	0.0169	7.8	19795	160	0.01	Hy	45	0.3
z220-1	18.3	1.3	18.5	3.5	n.s.		OR	0.00284	7.2	0.0184	19.3	5787	307	0.05	Hy	14	1.4
z225-3	18.9	1.3	20.8	2.4	n.s.		R	0.00293	6.8	0.0207	11.9	13827	51	<0.01	Hy	35	0.7
z239-2	20.0	1.3	20.9	1.9	n.s.		R	0.00311	6.6	0.0208	9.4	9725	33	<0.01	Me	26	1.0
z244-1	21.7	1.4	13.1	6.4	n.s.		C	0.00337	6.2	0.013	20.6	1379	119	0.09	Hy	4	1.9
z236-2	22.2	1.4	22.5	1.8	n.s.		R	0.00345	6.5	0.0224	8.1	16522	113	0.01	Hy	49	0.4
z227-2	25.2	1.7	25.4	2.7	n.s.		(OR)	0.00392	6.7	0.0254	10.8	16711	159	0.01	Hy	57	0.7
z220-2	170	14	180	27	315	320	C	0.02673	8.1	0.1942	16.5	555	99	0.18	Ma	13	-
z225-1	256	21	624	42	2368	53	C	0.04049	8.4	0.8485	9.0	2000	155	0.08	Ma	70	9.8
z238-1	343	19	350	19	437	56	OR	0.05463	2.9	0.4121	3.3	1042	240	0.24	Ma	49	2.1
z231-1	474	27	480	31	554	120	C	0.07637	5.8	0.6048	8.2	679	188	0.29	Ma	45	0.3
z210-1	622	49	1417	69	2962	54	C	0.10135	8.3	3.0387	9.0	478	86	0.19	Ma	42	12.6
z227-1	891	54	917	43	981	60	C	0.14816	6.5	1.4672	7.2	949	311	0.34	Ma	121	0.2
z219-2	1018	61	1240	49	1650	42	C	0.17101	6.5	2.3915	6.8	767	421	0.57	Ma	113	3.6
z239-1	1542	88	1642	55	1773	36	C	0.27021	6.4	4.0398	6.7	712	203	0.29	Ma	166	1.8
z216-1	1805	90	2066	51	2342	18	OC	0.32286	5.7	6.6488	5.8	541	219	0.42	Ma	150	1.2
z236-1	2271	130	2350	69	2419	54	C	0.42231	6.8	9.1145	7.5	101	214	2.19	Ma	37	2.9

[a]Similar caption as Table 2.

Table 5. C32 (= K1C32 of *Lacassin et al.* [2004a]) and C43 ID-TIMS U–Pb Isotope Data for Monazite (m) and Zircon (z)[a]

#	Fraction, μm	Wt., mg	U, ppm	Pb*, ppm	206Pb/204Pb (Atomic)	208Pb/206Pb	206Pb/238U (Ratios)	207Pb/235U	207Pb/206Pb	206Pb/238U (Apparent ages)	207Pb/235U	207Pb/206Pb	correl. coeff.
							C32 Leucocratic Dyke						
z1	<100 [24] need.cl.un.	0.055	5,224	16.4	2542	0.0722	0.00353 ±1	0.0227 ±1	0.0502 ±3	22.7	22.8	204	0.59
z2	<100 [19] need.cl.un.	0.034	4,031	23.5	2945	0.0819	0.00602 ±2	0.0441 ±3	0.0531 ±3	38.7	43.8	331	0.62
z3	>100 [8] sp.pi.un.	0.112	1,688	12.1	3318	0.0936	0.00726 ±2	0.0583 ±3	0.0582 ±2	46.6	57.5	538	0.67
z4	>100 [8] sp.pi.ab.	0.032	4,577	40.3	699	0.144	0.00822 ±2	0.0692 ±5	0.0610 ±4	52.8	67.9	640	0.49
z5	>100 [13] sp.pi.ab.	0.032	3,593	32.9	4346	0.1015	0.00942 ±2	0.0840 ±3	0.0647 ±2	60.4	81.9	763	0.68
m1	<100 [8] ye.an.	0.038	10,531	93.2	489	2.6295	0.00245 ±3	0.0156 ±2	-	15.7	15.7	-	0.91
m2	<100 [5] ye.an.	0.028	7,475	84.2	449	3.6697	0.00246 ±1	0.0158 ±1	-	15.9	15.9	-	0.78
							C43 Leucocratic Orthogneiss						
m1	<100 [4] ye.an.	0.025	15,106	78.6	785	1.2583	0.00222 ±1	0.0142 ±1	-	14.3	14.3	-	0.77
m2	<100 [5] ye.an.	0.029	19,557	86.2	993	0.9096	0.00220 ±1	0.0141 ±1	-	14.2	14.2	-	0.85

[a]Similar caption as Table 2. [] Number of grains of the analyzed fraction. ab. = air abraded, an. = anhedral, cl. = colorless, lp. = long prismatic, need. = needle shaped (acicular), pi. = pink, sp. = short prismatic, un. = unabraded, ye. = Yellow. The ± numbers represent the errors made on the last digit.

Table 6. Leucocratic Mylonite P34 Zircon SHRIMP II Data[a]

| Spot Name	Age, Ma 206/238	±(2σ)	Age, Ma 207/235	±(2σ)	Age, Ma 207/206	±(2σ)	CL Domain	206/238	±%	207/235	±%	U, ppm	Th, ppm	Th/U	Type	206Pb[a] ppm	% com Pb
z147-2	18.2	1.2	20.6	3.0	n.s.		OR	0.00283	6.7	0.0205	11.4	1362	86	0.07	Hy	3	0.9
z120-2	20.0	1.2	21.2	2.7	n.s.		OR	0.00311	6.0	0.0211	10.2	2542	15	0.01	Hy	7	0.6
z120-1	20.9	2.2	-	-	n.s.		ReC	0.00324	9.3	-	-	230	2	0.01	Me	1	1.4
z147-3	23.8	1.5	22.3	6.7	n.s.		OR	0.00369	6.1	0.0222	11.7	2057	121	0.06	Hy	7	1.1
z156-2	26.2	1.7	26.1	4.3	n.s.		(O)R	0.00407	6.4	0.026	10.7	2479	106	0.04	Hy	9	1.5
z122-2	26.9	1.6	22.9	4.4	n.s.		(O)R	0.00419	6.0	0.0228	9.6	1776	54	0.03	Hy	6	0.2
z147-1	270	16	296	22.7	611	91	C	0.04277	5.9	0.3387	7.3	509	64	0.13	Ma	19	0.9
z156-1	287	18	310	48	774	210	C	0.0456	6.2	0.3565	12.0	171	143	0.86	Ma	7	6.1
z145-3	317	21	414	180	1047	1000	OR	0.05032	6.8	0.5033	50.9	879	85	0.1	Ma	42	10.2
z145-1	331	31	352	32.2	546	110	OR	0.05271	9.6	0.4146	10.8	1063	106	0.1	Ma	48	0.0
z153-1	336	20	332	55.5			C	0.05357	5.9	0.3864	16.7	446	196	0.45	Ma	21	3.0
z122-1	477	27	692	38	1509	89	C	0.07681	5.8	0.977	7.5	335	87	0.27	Ma	22	5.4
z125-1	546	33	701	46.2	1325	87	ReC	0.08843	6.3	0.9941	7.8	1280	187	0.15	Ma	98	1.7
z122-3	573	32	876	45	1777	86	C	0.09295	5.9	1.3688	7.6	270	85	0.33	Ma	22	6.9
z144-1	700	39	802	36.5	1138	55	C	0.11461	5.9	1.203	6.6	641	120	0.19	Ma	63	0.6
z145-2	764	43	799	40.8	942	85	OC	0.12584	6.0	1.1972	7.3	496	165	0.34	Ma	54	1.9
z124-1	1105	59	1229	45.9	1485	50	C	0.18703	5.8	2.3562	6.4	254	106	0.43	Ma	41	0.9

[a]Same caption as Table 2. Re, recrystallized.
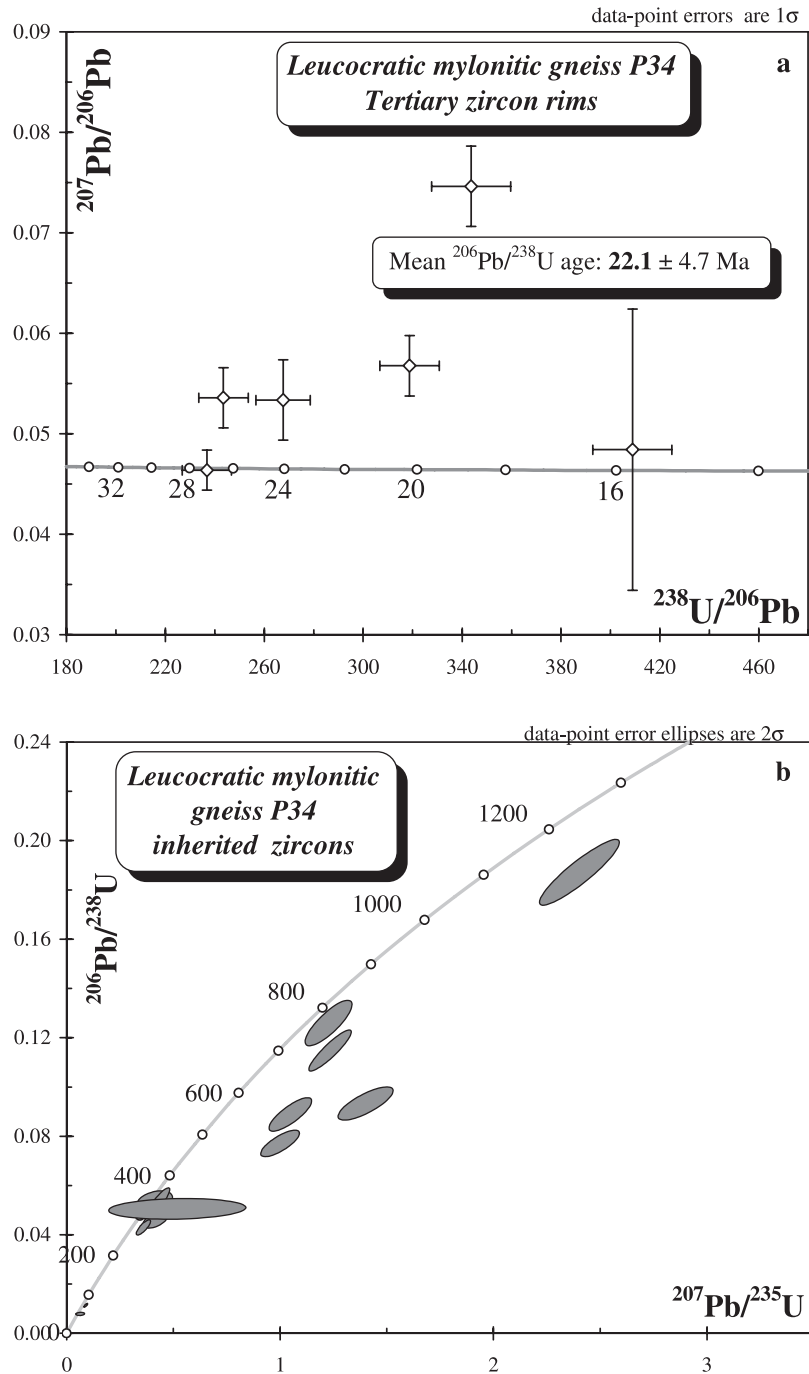
Figure 8. U-Pb SHRIMP II ages of leucocratic mylonitic orthogneiss P34 zircons (section 2, Figures 2, 3d, and Table 6). Same caption as Figure 7.

Table 7. Sheared Two-Mica Granitoid P18 Zircons SHRIMP II Data[a]

| Spot name	Age, Ma 206/238	±(2σ)	Age, Ma 207/235	±(2σ)	Age, Ma 207/206	±(2σ)	CL Domain	206/238	±%	207/235	±%	U, ppm	Th, ppm	Th/U	Type	206Pb[a], ppm	% com Pb
z1-1	19.8	1.4	23	3.0	n.s.		OR	0.00307	7.0	0.0229	13.2	2715	27	0.01	Ma-Me	7	1.2
z3-2	20.3	1.7	30.5	8.3	n.s.		OR	0.00315	8.4	0.0305	27.6	2198	204	0.1	Ma	6	2.1
z34-2	21.1	1.4	25.8	6.3	n.s.		OR	0.00327	6.7	0.0258	24.5	3292	1305	0.41	Ma	9	2.9
z53-2	21.6	1.5	23.1	7.6	n.s.		R	0.00336	7.0	0.0231	33.4	2733	407	0.15	Ma	8	4.5
z3-3	22.2	1.5	25.2	2.8	n.s.		OR	0.00346	6.7	0.0251	11.3	4883	240	0.05	Ma-Me	15	1.4
z25-2	22.8	1.6	30.6	4.0	n.s.		OR	0.00354	7.1	0.0306	13.2	3139	510	0.17	Ma	10	2.6
z41-3	23.3	1.8	25.7	15.3	n.s.		OR	0.00362	7.9	0.0256	60.2	2522	376	0.15	Ma	8.2	3.9
z30-2	24.4	1.8	28.4	13.0	n.s.		R	0.00379	7.3	0.0283	46.4	3722	503	0.14	Ma	12	3.1
z34-3	25.2	1.9	28.1	9.4	n.s.		OR	0.00391	7.5	0.0281	33.8	4762	853	0.19	Ma	16	3.0
z1-4	26.8	1.8	25.5	2.9	n.s.		OR	0.00416	6.6	0.0255	11.4	3171	49	0.02	Ma-Me	11	0.8
z8-2	27.3	2.0	27.1	11.5	n.s.		(O)R	0.00424	7.3	0.0271	42.9	1525	282	0.19	Ma	6	3
z53-3	27.4	1.9	26.3	7.1	n.s.		OC	0.00426	6.9	0.0263	27.4	5617	742	0.14	Ma	21	2.4
z41-1	32.7	2.3	31.9	8.2	n.s.		OC	0.00508	7.1	0.0319	26.1	2237	3026	1.4	Ma	10	2.7
z41-2	34.8	2.2	38.8	3.0	n.s.		OC	0.00541	6.5	0.0389	7.9	5857	1174	0.21	Ma	27	0.2
z8-1	35.9	2.5	38.6	11.9	n.s.		OC	0.00559	6.9	0.0388	31.3	2349	611	0.27	Ma	12	2.4
z18-2	44.8	3.0	56.8	15.7	n.s.		C-R	0.00697	6.8	0.0575	28.5	1807	164	0.09	Ma-Me	11	2.9
z34-1	181	13	198	75	415	900	C	0.0284	7.0	0.2156	41.6	381	98	0.27	Ma	10	3.5
z53-1	294	19	302	56	367	450	C	0.04658	6.7	0.3462	21.4	321	136	0.44	Ma	13	1.9
z1-5	325	29	416	72	958	380	OC	0.05171	9.0	0.5064	21.0	210	114	0.56	Ma	9.4	-
z18-1	396	25	425	44	590	230	C	0.06328	6.6	0.5202	12.5	551	299	0.56	Ma	30	1.8
z25-1	438	27	484	29	709	79	C	0.07024	6.4	0.6103	7.5	869	310	0.37	Ma	53	0.9
z30-1	442	28	461	38	555	170	C	0.07104	6.6	0.5746	10.2	365	179	0.51	Ma	22	1.3
z3-1	736	48	800	57	984	150	C	0.12095	6.9	1.1997	10.3	198	143	0.75	Ma	21	1.6
z48-1	1771	106	1802	104	1837	180	C	0.31625	6.9	4.8964	12.3	159	106	0.69	Ma	43	1.8

[a]Same caption as Table 2.
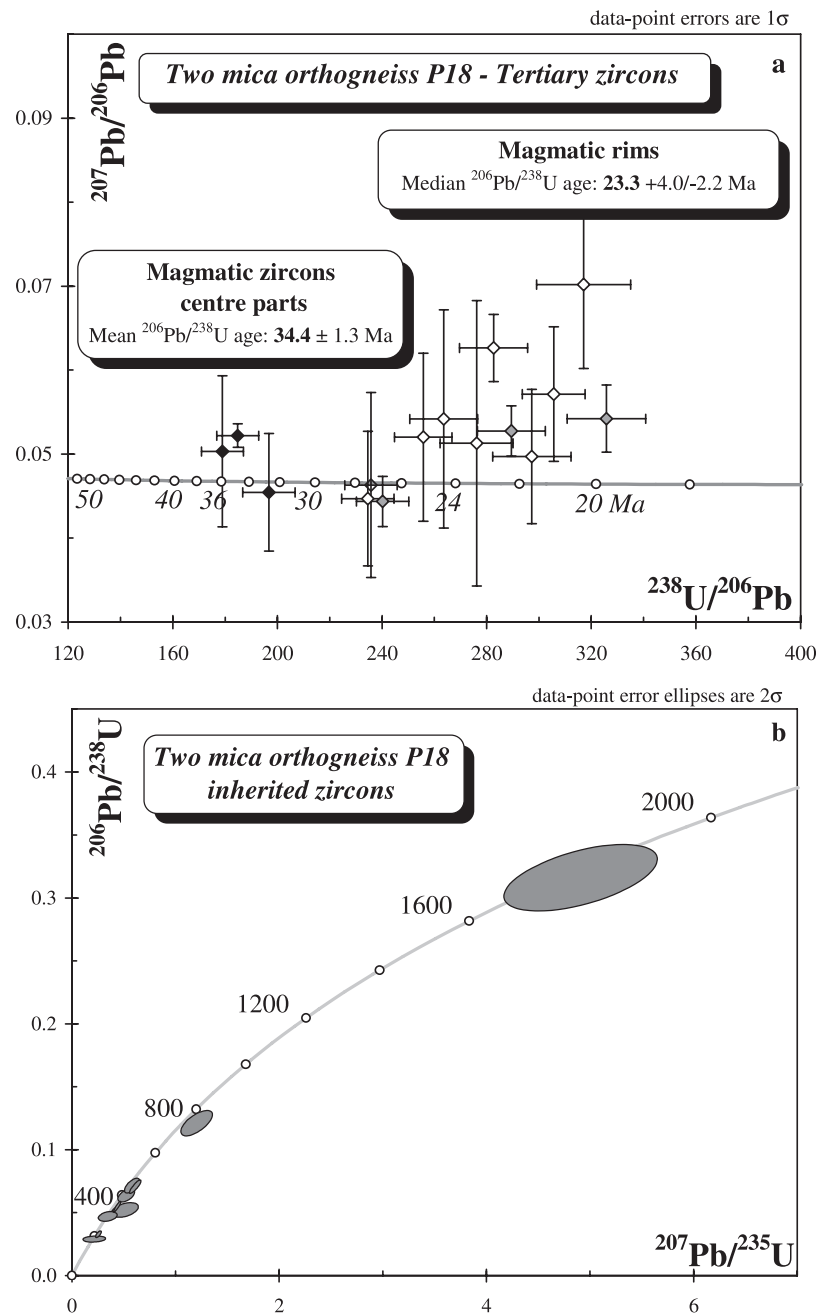
Figure 9. U-Pb SHRIMP II results of zircons from the two-mica orthogneiss P18 (section 3, Figures 2, 3c, and Table 7). (a) Tertiary zircon ages plotted in a Tera-Wasserburg diagram; white and black diamonds correspond to zircon rims and the central part of uniformly zoned grains respectively; grey diamonds correspond to metamorphosed magmatic rims. (b) Ages of CL bright zircon cores plotted in a $^{206}Pb/^{238}U$ versus $^{207}Pb/^{235}U$ concordia diagram.
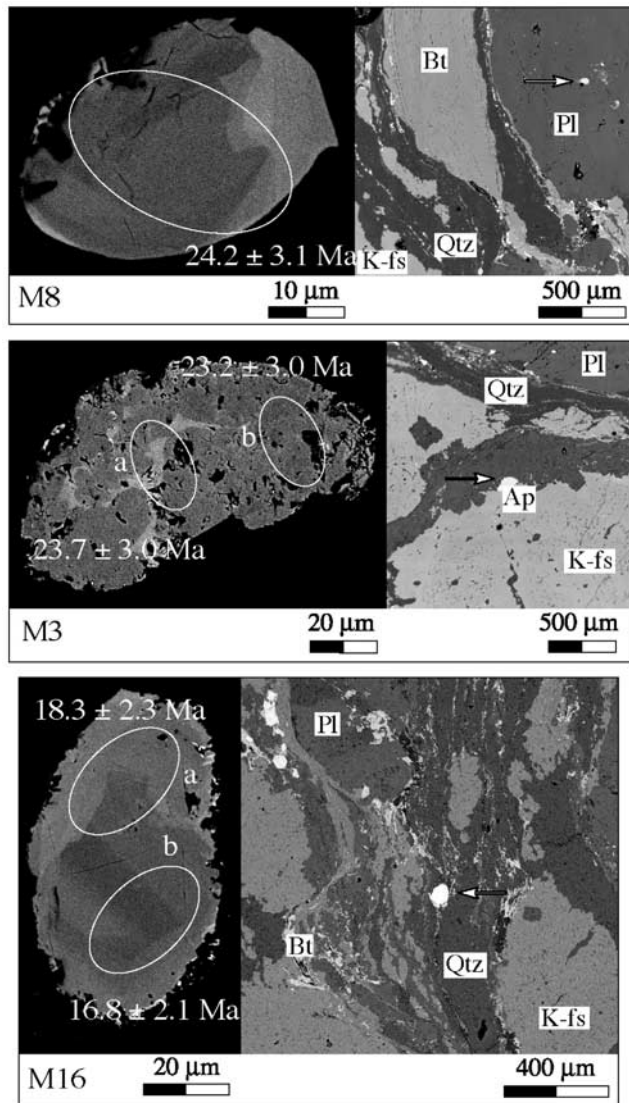
Figure 10. BSE images of monazites from the two-mica orthogneiss P18 (section 3, Figures 2, 3c, and Table 8). Right, view of monazite surroundings, arrows point towards monazite location in the thin sections. Ap, apatite; Bt, biotite; K-fs, K-feldspar; Qtz, quartz; Pl, plagioclase. Left, detail of monazite crystals with ion probe spots and corresponding $^{208}Pb/^{232}Th$ ages (2σ error, Table 8).

the result of partial melting of a ~33 Ma old magmatic intrusion. The upper intercept at ~1300 Ma is poorly defined by discordant fractions and may reflect either a single crystallization event or the average of a complicate inheritance pattern.

[36] Two monazite fractions were dated by ID-TIMS (m1 and m2, Table 5). The concordant, slightly overlapping analytical ellipse errors yield a mean age of 15.8 ± 0.2 Ma (2σ) (Figure 13). This implies the primary crystallization of newly formed hydrothermal or metamorphic monazite crystals or the resetting of older magmatic grains within the leucogranite C32 at that time.

4.4. Labhar Kangri Granite K2P30

[37] In sample P30, the zircons are colorless and translucent needle-shaped crystals, as well as elongated light pink and yellow short-prismatic euhedral grains. Six fractions were selected for ID-TIMS dating (Figure 14). One fraction of acicular grains yield a concordant age of 21.1 ± 0.3 Ma (Table 10), comparable to those measured on westernmost granitoids from the Ayilari range. The five remaining fractions are discordant and indicate two different inherited component with upper intercept ages at 494 ± 45 Ma and 1447 ± 38 Ma.

5. Summary and Discussion

5.1. Summary of U-Th-Pb Data in the NA Range

[38] All U-Th/Pb ages obtained in the Ayilari range are summarized in Table 11 and Figure 15. All samples unless P20 reveal at least three magmatic or metamorphic / metasomatic episodes. All samples record Cenozoic ages comprised between 35 and 14 Ma. The age inheritance patterns derive from several events spanning a long period between the late Archean (~3 Ga) and the Jurassic (~170 Ma). Three samples (C32, P18, and L89) indicate an Eocene-Oligocene (~35−32 Ma) magmatic episode. These three samples also show a younger Oligo-Miocene magmatic event for which populations of monazite and zircon grains yield average ages between ~25 and 23 Ma. This magmatic event is also indicated by P20 zircons (21.7 ± 3.6 Ma). A ~25−22 Ma magmatic event is thus recorded in most samples of the NAsz.

[39] In samples P34 and C43, metamorphic zircons, characterized by low or intermediate U/Th ratio and U-contents, crystallized around 21 Ma. Hydrothermal zircons characterized by high to very high U-content, and very low U/Th ratio crystallized between ~22 and 17 Ma while monazite populations in samples L89, P34, C32, P18, and C43 yield ages between ~19 and ~14 Ma. We interpret these ages as the result of metamorphism and metasomatism either during several pulses during the ~22−14 Ma time period, or as a single ~14 Ma event producing partial Pb loss and discordance of the analytical points.

[40] The cooling history of the NA range is constrained by Ar/Ar, U-Th/He and fission track data (Figure 16) [*Valli et al.*, 2007; *Lacassin et al.*, 2004a]. These data reveal rapid cooling below ~350°C starting at ~15 Ma along section 1 and at ~13 Ma in all other sections. Such cooling history fits well with the fact that no zircon, nor monazite populations, gives U-Th/Pb age younger than ~14 Ma.

[41] The picture that emerges is that major Oligo-Miocene (23.4 ± 1.4 Ma) magmatic, event(s) affected rocks containing Eocene-Oligocene and pre-Mesozoic inherited zircons. These rocks were then affected by metamorphism and metasomatism, and after ~15 Ma rapidly cooled below 350°C (Figure 16).

5.2. Age of Deformation in the Ayilari Range

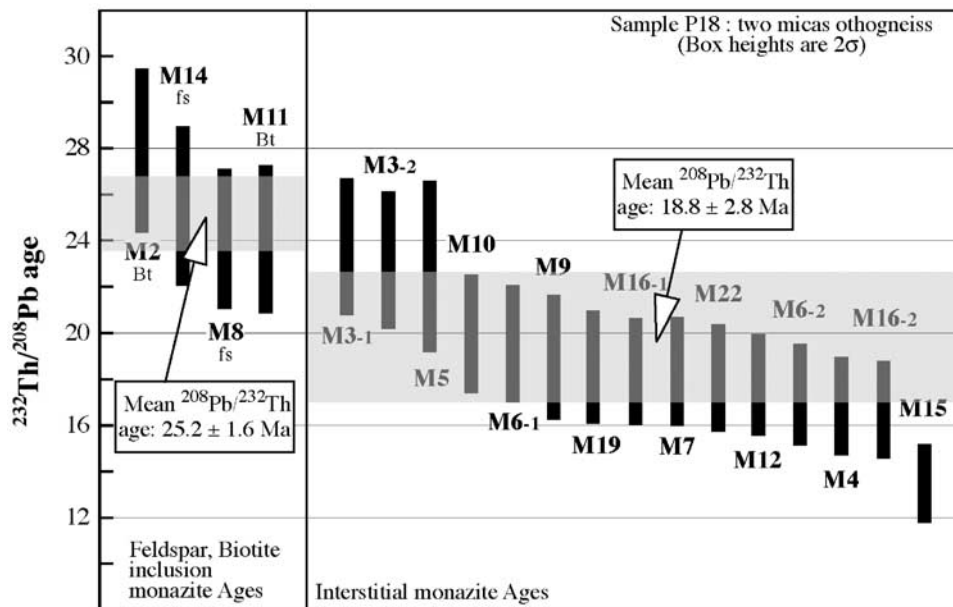[42] Because C32 leucocratic dyke is synkinematic to the right-lateral deformation (see section 2.3, Figures 3e,

Figure 11. ^{208}Pb/^{232}Th ages from in situ IMS 1270 microprobe dating of monazites in the two-mica orthogneiss P18 (section 3, Figures 2, 3c, and Table 8). Caption similar to Figure 7.

3f, and 3g), *Lacassin et al.* [2004a, 2004b] inferred that deformation started prior to the emplacement of that dyke. At a larger scale, the fact that numerous undeformed leucocratic dykes cut across the deformed migmatites (Figure 3a) corroborate that such dykes postdate the onset of deformation in the NAsz. An age of 22.7 ± 0.1 Ma is given to C32 by the youngest concordant zircon fraction it contains (Figure 13 and Table 5). This age is a lower bound for the onset of right-lateral shear.

[43] The three other samples that record Oligo-Miocene magmatism (L89, P18, and P20) have been affected by ductile deformation related to the NAsz. Their U/Pb ages spanning from 25 to 21 Ma could thus be interpreted as an upper bound for the onset of shearing (i.e., the age of the protolith prior to deformation). However, the fact that these ages are identical within errors to that of C32 (Figure 15), and that S-C fabrics, typical of shear under high to medium-grade temperature conditions and often of syn-kinematic granitoid [e.g., *Gapais*, 1989a, 1989b; *Gapais and Barbarin*, 1986],

Table 8. Sheared Two-Mica Granitoid P18 Monazite SHRIMP II Data[a]

Spot Name	Age, Ma 208/232	±(2σ)	208/232	±%	Th, Wt%)	U, ppm	Th/U Wt	208Pb[a], ppm	% com 208Pb	Structural Location
m15	13.5	1.7	0.000666	12.7	7.8	2026	31	52	1.3	It
m16-b	16.8	2.1	0.000826	12.6	4.6	545	18	38	24.5	It
m4	16.9	2.1	0.000835	12.7	7.1	5214	14	59	4.8	It
m6-b	17.4	2.2	0.000859	12.7	8.5	2021	18	73	0.7	It
m12	17.7	2.2	0.000876	12.6	2.1	531	65	18	3.9	It
m22	18.1	2.4	0.000894	13.1	8.8	2648	21	79	2.4	It
m16-a	18.3	2.3	0.000906	12.7	7.4	1844	44	67	1.3	It
m7	18.3	2.3	0.000908	12.7	10.2	1640	29	92	0.3	It
m19	18.5	2.3	0.000917	12.6	5.1	977	51	47	0.6	It
m9	19.3	2.7	0.000939	14.2	6.2	586	62	58	56.9	It
m6-a	19.5	2.5	0.000964	12.9	8.5	2021	26	82	0.7	It
m10	19.9	2.6	0.000986	12.9	8.9	2439	26	87	3.1	It
m5	23.0	3.7	0.001137	16.2	8	1889	33	91	0.1	It
m3-b	23.2	3.0	0.001148	12.8	8.4	2562	24	97	1.1	It
m3-a	23.7	3.0	0.001174	12.6	7.4	1939	16	87	0.1	It
m11-a	24.1	3.1	0.001193	13.0	8.1	5428	17	97	0.1	Ic Bt
m8	24.2	3.1	0.001196	12.6	7.2	1631	30	86	2.4	Ic Fs
m14	25.5	3.5	0.001263	13.5	8.6	5024	24	108	0.2	Ic Fs
m2	27.9	3.6	0.001383	12.8	9.3	1040	60	128	0.1	Ic Bt

[a]Same caption as Table 2.

Table 9. Sheared Biotite-Rich Granitoid P20 Zircon Cameca IMS 1270 Data[a]

Spot Name	Age, Ma 206/238	±(2σ)	Age, Ma 207/235	±(2σ)	Age, Ma 207/206	CL Domain	206/238	±%	207/235	±%	U, ppm	Th, ppm	Th/U		206Pb[a], ppm	% com Pb
z23	19.9	1.6	24.6	6.1	n.s.	n.d.	0.00309	8.2	0.0245	25	3882	5514	1.42	Ma	10	5.5
z24	20.1	1.2	20.9	1.5	n.s.	n.d.	0.00313	6.2	0.0208	7.4	2523	777	0.31	Ma	7	0.2
z18	21.2	1.3	21.9	1.5	n.s.	O	0.0033	6.4	0.0218	7.0	1640	909	0.55	Ma	5	0.2
z27-2	23.6	1.6	25.0	3.7	n.s.	n.d.	0.00367	6.8	0.0249	14.8	1014	258	0.25	Ma	3	1.8
z27-1	23.9	6.9	22.6	49.1	n.s.	n.d.	0.00371	29.2	0.0225	219	1750	274	0.16	Ma	6	22.2

[a]Similar caption as Table 2.

are ubiquitous in the NAsz (Figure 3), suggest that migmatisation (L89) and Oligo-Miocene magmatism (P18 and P20) are at least partly synkinematic. This implies that the magmatic ages of these rocks do not provide a strict upper bound, but that deformation started some time during or prior to the Oligo-Miocene magmatic episode at 22–25 Ma. On the other hand, there is no clear argument to link the older Eocene-Oligocene phase of magmatism seen in samples L89, C32, and P18 (35–32 Ma) to right-lateral deformation deformation along the KFZ.

[44] These conclusions are in agreement with the cooling histories based on Ar/Ar data that suggest that the shear zone temperature dropped below 400°C before 15 to 21 Ma depending on the samples considered (Figure 16) [*Valli et al.*, 2007], thus implying that ductile deformation was chiefly acquired prior to 21 Ma at least for some part of the shear zone. This interpretation is however strongly contested by authors that consider that there is no evidence

for synkinematic partial melting, and thus that right-lateral shear should have started after, not before, ∼21 Ma [*Searle and Phillips*, 2004, 2007]. The crucial point in that controversy is that the crosscutting dykes are clearly syn to late kinematics (C32 see Figure 3) and dated at 22.7 ± 0.1 Ma (Figure 13), implying that deformation started before that time. Postponing the onset of ductile deformation in NAsz would imply (1) to contest the age of C32, (2) to infer that temperatures stayed above 400°C more recently than suggested by the Ar data and (3) to provide an alternative explanation for the ages of metamorphic and metasomatic zircons and monazites that fill the gap between the last magmatic event and the onset of rapid cooling linked with right-lateral / normal deformation.

[45] The most straightforward interpretation of our data is thus to confirm the analysis of *Lacassin et al.* [2004a, 2004b] that links the Oligo-Miocene magmatism, and the following metamorphism and fluid circulation in the NA
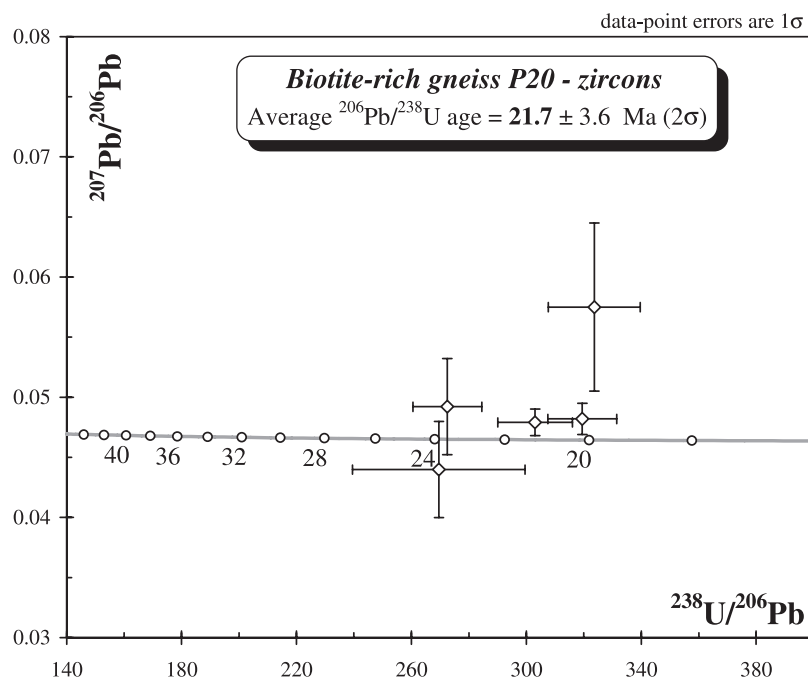

Figure 12. Tera-Wasserburg diagram of IMS1270 in situ analyses of zircons from the biotite-rich gneiss P20 (section 3, Figure 2, and Table 9).
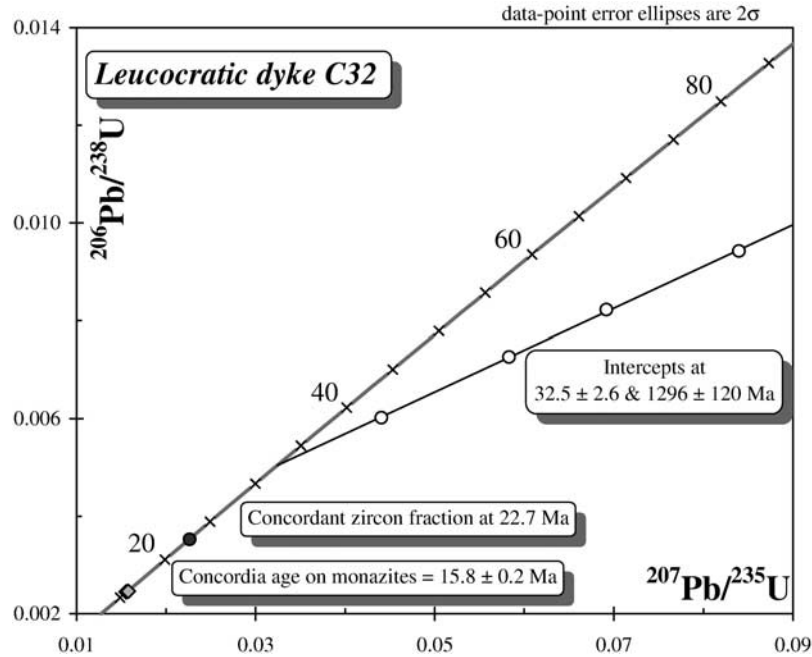
Figure 13. Concordia diagram of ID-TIMS conventional multigrain analysis of zircons (white and grey circles) and monazites (grey diamonds) from the crosscutting leucocratic dyke C32 (section 3, Figures 2 and 3f). Errors smaller than symbols. See data in Table 5.

range to right-lateral shear in the Karakorum shear zone. Metamorphism and fluid advection is typical of major strike-slip shear zones as documented in several natural examples [e.g., *Leloup et al.*, 1999, and references therein; *Moore et al.*, 2001]. This in turns implies that right-lateral

deformation initiated at high temperature in the NAsz prior to ~22 Ma, probably during or just prior to the 25–22 Ma magmatic episode. The deformation pursued under decreasing temperature conditions until ~300°C were reached ~15
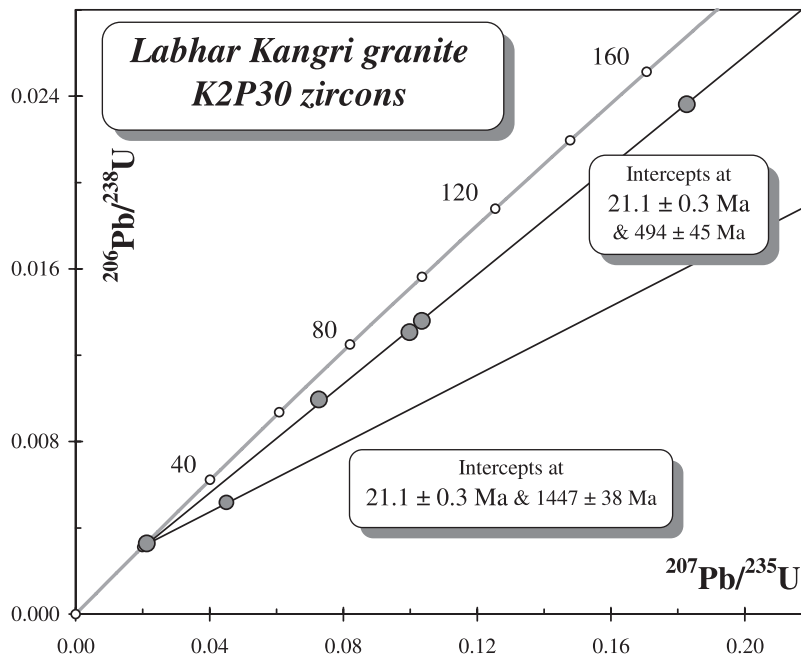

Figure 14. Concordia diagrams (^{206}Pb/^{238}U versus ^{207}Pb/^{235}U) of ID-TIMS multigrain analysis of zircons from the Labhar Kangri granite K2P30 (Figure 1, and Table 10).

Table 10. K2P30 ID-TIMS U–Pb Isotope Data for Zircon[a]

n°	Fraction, μm	Wt, mg	U, ppm	Pb rad, ppm	^{206}Pb/^{204}Pb	^{208}Pb/^{206}Pb Atomic	^{206}Pb/^{238}U Ratios	^{207}Pb/^{235}U Ratios	^{207}Pb/^{206}Pb	^{206}Pb/^{238}U Apparent Ages	^{207}Pb/^{235}U Apparent Ages	^{207}Pb/^{206}Pb Apparent Ages	correl. coeff.
1	>100 [21] need.cl.un.	0.192	691	2.42	434	0.1663	0.00328 ± 3	0.0213 ± 5	0.0471 ± 9	21.1	21.4	53	0.52
2	>150 [5] lp.pi.un.	0.23	598	3.35	809	0.1558	0.00518 ± 1	0.0451 ± 1	0.0632 ± 1	33.3	44.8	713	0.83
3	>150 [4] lp.pi.un.	0.107	1,238	12.2	1957	0.0896	0.00994 ± 2	0.0727 ± 2	0.0530 ± 1	63.8	71.2	329	0.82
4	>150 [7] sp.ye.un.	0.241	833	10.9	2023	0.0968	0.01306 ± 5	0.0998 ± 4	0.0554 ± 1	83.6	96.6	430	0.88
5	>150 [8] sp.ye.un.	0.246	811	11.2	1682	0.1105	0.01359 ± 4	0.1034 ± 3	0.0552 ± 1	87.0	99.9	421	0.86
6	>150 [6] sp.ye.ab.	0.178	614	14.5	1461	0.0929	0.02362 ± 7	0.1826 ± 8	0.0561 ± 1	150.5	170	456	0.76

[a]Same caption as Table 5.

Table 11. Summary of ID-TIMS, SHRIMP II and Cameca IMS 1270 Ages[a]

Transect	1	1	2	3	3	3	3	3	4	4	Labhar Kangri
Samples	Migmatitic Gneiss **L89**	Migmatitic Gneiss **L89**	Leucocratic Orthogneiss **P34**	Two-Mica Orthogneiss **P18**	Two-Mica Orthogneiss **P18**	Biotite-Rich Gneiss **P20**	Leucocratic Dyke **C32**	Leucocratic Dyke **C32**	Leucocratic Orthogneiss **C43**	Leucocratic Orthogneiss **C43**	Granite **K2P30**
Method	SHRIMP II	SHRIMP II	SHRIMP II	SHRIMP II	IMS-1270	IMS-1270	ID-TIMS	ID-TIMS	SHRIMP II	ID-TIMS	ID-TIMS
Mineral	Zircon	Monazite	Zircon	Zircon	Monazite	Zircon	Zircon	Monazite	Zircon	Monazite	Zircon
Inheritance	~300–2620 [15]	>150 [2]	~300–1800 [11]	~180–1800 [8]			~1300 [4]		~170–3000 [10]		~490–1450 [5]
Magmatic	**34.7 ± 2.4** [1]			**34.4 ± 1.3** [3]			**32.5 ± 2.6** [4]				
Magmatic	**23.4 ± 4.0** [1]	**24.2 ± 2.4** (25.4 – 23.1 +3.6, –6.9) [3]	**22.1 ± 4.7** (26.9 – 18.2 +1.6, –1.2) [6]	**23.3 +4 –2.2** (27.4 – 19.8 +1.9, – 1.7) [9]	**25.2 ± 1.6** (27.9 – 24.1 +3.6, –3.1) [4]	**21.7 ± 3.6** (23.9 – 19.9 +6.9, –1.6) [5]	**22.7 ± 0.1** [1]				
Metamorphic or hydrothermal		**18.2 ± 1.8** (21.8 – 13.1 +2.6, –5.1) [10]			**18.8 ± 2.8** (23.7 – 13.5 +3.0, –1.7) [15]			**15.8** ± 0.2 [2]	**21.7** ± 1.4 [1]	**14.4 ± 0.7** [2]	**21.1** ± 0.3 [1]
Metamorphic or hydrothermal									**17.8** +4.4 –3.4 (25.2 – 13.1 +1.7, –0.8) [10]		

[a] Average ages in Ma of zircon/monazite grains populations are reported in bold with the corresponding 95% confidence level error (xx.x – xx.x) with extremum 2σ errors (+x.x, –x.x) and number of individual ages [n] are also given. Magmatic and, metamorphic / Hydrothermal zircons are distinguished from their crystal shape, color, Th/U ratio, U content and BSE – CL patterns, see text for details.
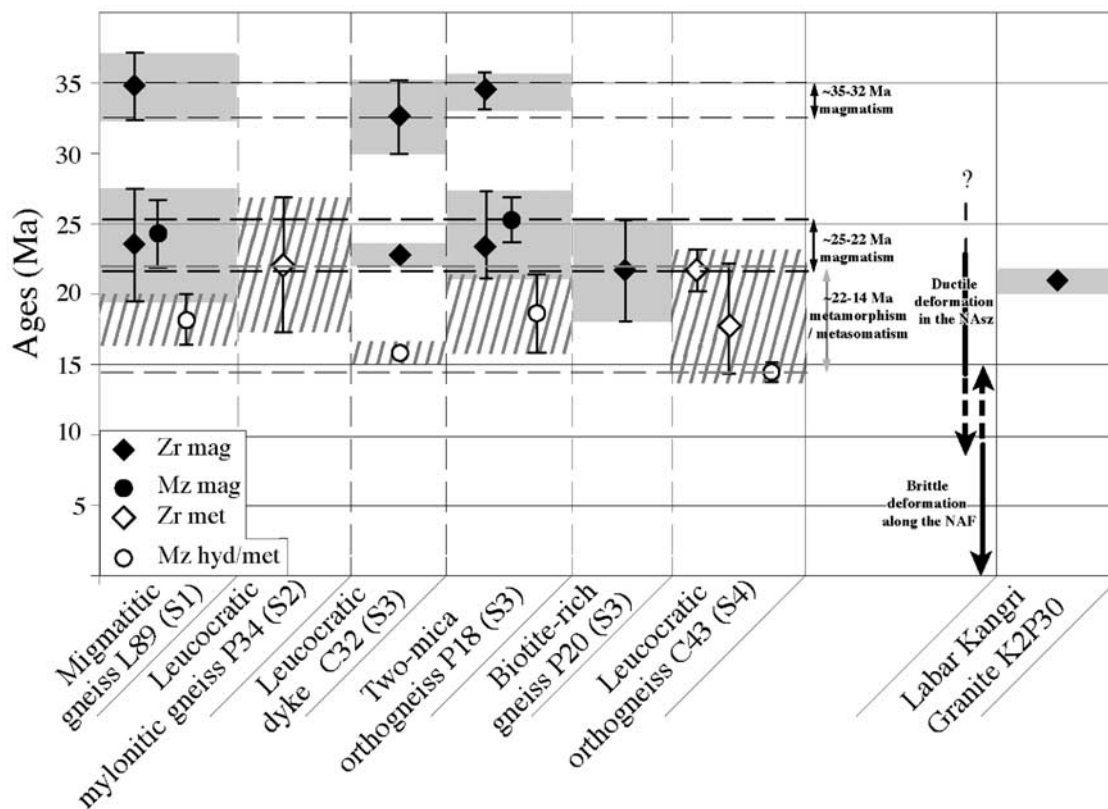
Figure 15. Summary of Tertiary U-Th-Pb results. North Ayilari shear zone on left and Labhar Kangri on right. Zircons mean ages appear as diamonds, and monazites as circles. Error bars are 2σ. No error bars are shown when they are smaller than symbol. Black and white diamonds are magmatic, and metamorphic/hydrothermal grains, respectively. Corresponding age ranges are respectively outlined by grey shade and hachure. See text sections 5.1 and 5.2 for details.

to 10 Ma ago [*Valli et al.*, 2007]. Since then right-lateral / normal brittle deformation occurs along the NAaf.

5.3. Insights Into Pre-Tertiary History of the Ayilari Rocks

[46] The Ayilari range is located in the southeastern prolongation of the Ladakh batholith (Figure 1) that emplaced between ∼103 and 50 Ma [e.g., *Schärer et al.*, 1983; *Weinberg and Dunlap*, 2000; *Schwab et al.*, 2004]. Surprisingly, despite the large number of analyzed zircons in our study (∼50) we did not find any inherited core recording such crystallization ages (Table 11). As already discussed, the age inheritance patterns of most samples are multigenetic with zircon grains being derived from several events spanning a long period between the Jurassic and the late Archean (between ∼170 and 3000 Ma) (Table 11, Figures 5, 7b, 8b, 9b, 13, and 14). This large age span together with the high mica content of the samples (between 13 and 40%) suggests that most of the Ayilari Range Tertiary granitoids initially derive from melting of metasedimentary rocks [*Chappell and White*, 1974], possibly through several melting episodes. This indirectly confirms that the eastern part of the Ladakh batholith emplaced on a continental basement as proposed by *Rolland et al.* [2000]

and *Rolland* [2002]. The youngest concordant zircon grain ages, older than the Ladakh batholith emplacement, are around 400 Ma. This age yield an upper bound for the deposition of the sediments constituting the protolith. Considering the Tertiary events as lower intercepts, discordant inherited zircons younger than ∼400 Ma broadly define a discordia line with this Early Devonian upper intercept (Figures 8b and 9b). This s.uggests a post Early Devonian deposition of the original sediments. In the absence of any Himalayan age, deposition probably took place prior to the emplacement of the Ladakh batholith. Such sediments possibly correspond to the Paleozoic-Mesozoic Tethyan series, which are actually outcropping on the Qiangtang and Lhasa blocks [*Jiao et al.*, 1988].

5.4. Timing of Onset of the KFZ: Conflicting Constraints From Various Places Along the Fault?

[47] Because the KFZ stands out as the main active strike-slip fault bounding the Tibetan plateau to the southwest its timing and slip history have been the subject of several studies. Various constraints on the timing of the fault onset have been proposed in different places. These constraints are summarized in Table 12 and Figure 17.
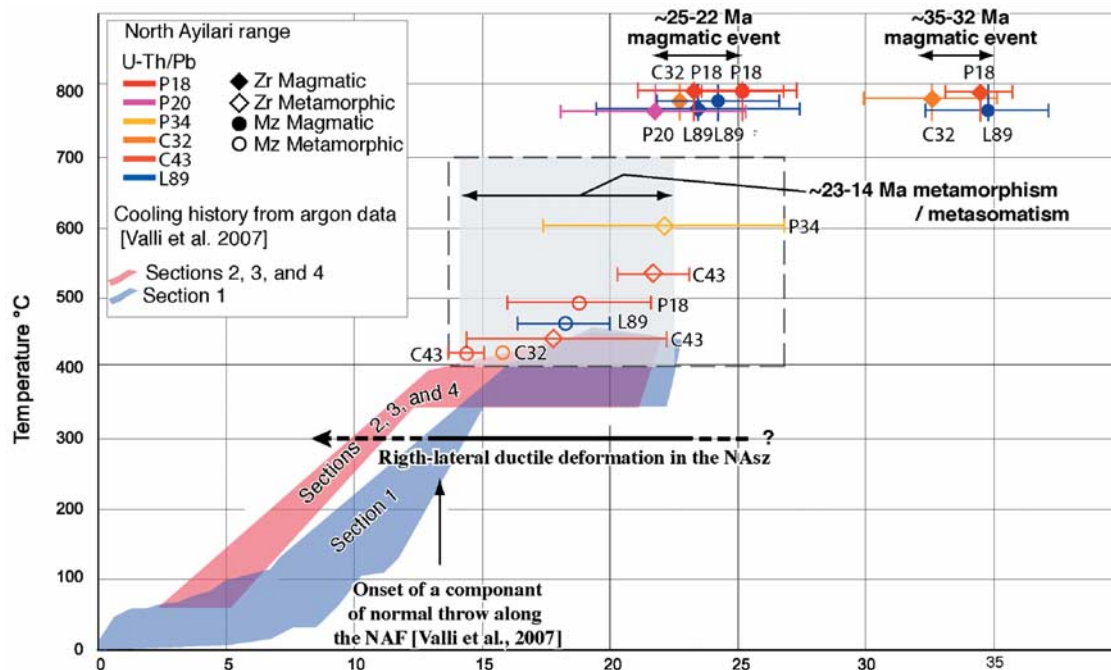
Figure 16. North Ayilari shear zone cooling history. U-Th/Pb ages (this study) and Ar/Ar-FT-U/He cooling histories [*Valli et al.*, 2007] plotted as a function of temperature. Ages are plotted with a 2σ confidence level. The magmatic zircons and monazites are taken as constraining granitoid crystallization at ca 750–800°C [*Clemens*, 2003]. Closure temperatures of metamorphic / metasomatic zircons and monazites are unknown within a 700–400°C range and could plot anywhere in the dashed box, most ages being within the gray area (see text for discussion).

[49] Along the Pangong and Nubra ranges (Figure 1), the KFZ was first thought to be younger than ~5 Ma [*Searle*, 1996]. Since then, the description of ductile deformation in these ranges, in a restraining bend between two strands of the KFZ, and the dating of granitoids led to propose older ages for the onset of deformation [e.g., *Searle et al.*, 1998]. By linking rapid cooling, starting at ~17 Ma according to cooling histories based on Ar data, with transpression along the fault *Dunlap et al.* [1998] proposed that motion on the KFZ started at that time ([3] on Figure 17 and Table 12). Considering that all granitoids, unless few late dykes, are strictly prekinematics, led to bracket the onset of right-lateral shear between 15.7 and 13.7 Ma ([1] and [2] on Figure 17 and Table 12), [*Phillips et al.*, 2004; *Searle and Phillips*, 2004, 2007; *Phillips and Searle*, 2007].

[50] Across the Baer basin, *Murphy et al.* [2000], propose that the South Kailas thrust has been offset 66 ± 5.5 km by the KFZ. The age of this thrust, deduced from the cooling history based on a single Kf Ar data from its footwall [*Yin et al.*, 1999], is ~13 Ma. This would constrain the KFZ to be younger than 13 Ma at this location ([9] on Figure 17 and Table 12).

[51] On the basis of the age constraints at Pangong and Baer, the KFZ might have started in Pangong at ~14 or 17 Ma and propagated to the SE reaching Baer less than 13 Ma ago ([A] on Figure 17, *Murphy et al.* [2000]). However, this would imply a shear onset after ~13 Ma in the NA range, which is in contradiction with our results ([6]

and [7] in Figure 17 and Table 12), (section 5.2) [see *Lacassin et al.*, 2004a, 2004b; *Valli et al.*, 2007]. It could thus be envisaged that the KFZ nucleated in the North Ayilari 25–22 Ma ago or before, prior to propagate north-westward, reaching Pangong after ~15.7 Ma, and south-westward reaching Baer after 13 Ma, thus reconciling previous interpretations ([B] on Figure 17). This would imply propagation rates on the order of 20 to 30 mm/a (northwestward), and ≤1 mm/a (southwestward). Such rates would be very low compared for example with the propagation rates of 138 to 200 mm/a inferred for the North Anatolian fault [*Armijo et al.*, 1999]. Furthermore, they would not allow the KFZ to reach its total length before present time. More complicated scenarios, such as variations in fault propagation rate or simultaneous initiation in distant parts of the fault cannot be ruled out, but remain conjectures given the dearth of data.

[52] To the contrary, there is evidence that the KFZ was active in Tangtse and Baer prior to ~15 and ~13 Ma respectively [*Lacassin et al.*, 2004a], implying an older history of the KFZ. According to *Murphy et al.* [2000, 2002] the KFZ ends southward in the Gurla Mandhata detachement system (GMDS) (Figure 1), implying that the KFZ started to slip less than 13 Ma ago in the Mt Kailas area. *Lacassin et al.* [2004a] showed that this hypothesis is implausible because (1) there is no demonstrable connection between the KFZ and the GMDS, the ophiolitic rocks in between being not significantly offset (Figure 1); (2) struc-

Table 12. Published Timing Constraints Ages of Shearing Onset and Miocene Magmatism Along the KFZ[a]

Onset Age of Right-Lateral Deformations Along the KFZ

Ref Figure 17	Age	Location	Type of age Constrain (Sample)	Reference	Inferences
[1]	between 15.9 and 13.7 Ma	nubra plutonic unit E77°37′–E77°45′	bracketed by the age of deformed (P38) and little deformed (P37) dykes	Phillips et al. [2004]	All protolithes of orthogneiss are stricktly synkinematic
[2]	between 15.6 and 13.7 Ma	Pangong range Tangtse E78°10′	bracketed by the age of deformed (P11) and little deformed (P8) dykes	Phillips et al. [2004]	All protolithes of orthogneiss are stricktly synkinematic
[3]	~17 Ma	Pangong range Tangtse E78°10′	Cooling history based on Ar data	Dunlap et al. [1998]	First phase of rapid cooling due to transpretional exhumation
[4]	prior to ~18 Ma	Pangong range Tangtse E78°10′	Age of the Tangtse granite and Pangong migmatites and granite (O22 and 215, Searle et al., 1998)	Rolland et al. [2008]	Tangtse granite and Pangong migmatites are synkinematic
[5]	prior to ~32 Ma	Pangong range Tangtse E78°10′	Amphibole oldest Ar steps (L450)	Rolland et al. [2008]	Pangong granulites are synkinematic
[6]	prior to ~23 Ma	North Ayilari (NA) sz E79°40′	age of syntectonic dyke (2nd magmatic episode, C32)	Lacassin et al. [2004a, 2004b]; this study	2nd phase (~25–22 Ma) of magmatism is synkinematic
[7]	prior to ~21 Ma	North Ayilari (NA) sz E79°40′	minimum age of ductile deformation from cooling history based on Ar data	Valli et al. [2007]	
[8]	prior to ~35 Ma	North Ayilari (NA) sz E79°40′	age of 1st magmatic episode in the NA range (L89, P18, C32)	Lacassin et al. [2004a, 2004b]	All Tertiary magmatic episodes are synkinematic
[9]	After ~13 Ma	Baer basin E80°30′	age of the South Kailas thrust from Ar cooling history [Yin et al., 1999]	Murphy et al. [2000]	South Kailas thrust antecedent to the KFZ

Magmatism

Ref Figure 17	Age	Location	Comment (Sample)	Reference
[M1]	20–18 Ma	W of Tash Gorgan	Alkali granite	Arnaud [1992]; Xie et al. [1992]
[M2]	25.5 ± 0.3 Ma	baltoro batolith ~E77°	1st pulse of magmatism (K11)	Schärer et al. [1990]
[M3]	21 ± 0.5 Ma	baltoro batolith ~E77°	2nd pulse of magmatism (K10, H4, H8)	Parrish and Tirrul [1989]; Schärer et al. [1990]
[M4]	~16–15 Ma	Nubra plutonic unit E77°37′–E77°45′	samples P38 and 021	Phillips et al. [2004]; Weinberg et al. [2000]
[M5]	18.5 ± 1.5 Ma	Pangong range Tangtse E78°10′	Tangtse granite (215) and Pangong migmatites (O22)	Searle et al. [1998]
[M6]	~25–22 Ma	North Ayilari (NA) E79°40′	2nd magmatic episode (P18, P20, P34, C32, C43 and L89)	this study
[M7]	21.1 ± 0.3 Ma	Labhar-Kangri	(K2P30)	this study

[a]Only the longitude along the fault is given for location. See Figure 17 and text sections 5.4 and 5.5.

tural mapping in the Kailas range rather indicates that most of the dextral motion is transferred east of the GMDS along the Yarlung Tsangpo suture zone; (3) the South Kailas thrust cannot be used as a marker to define a piercing point because it is a part of the KFZ flower structure mapped in this area. The 13 Ma age derived for this thrust [*Yin et al.*,

1999] is thus only an evidence for KFZ activity at that time. It is thus probable that the KFZ initiated in Baer prior to 13 Ma ago.

[53] Other lines of evidence also concur to suggest that the Tangtse shear zone in the Pangong area was active prior to ~16 Ma. (1) Several generations of variously deformed
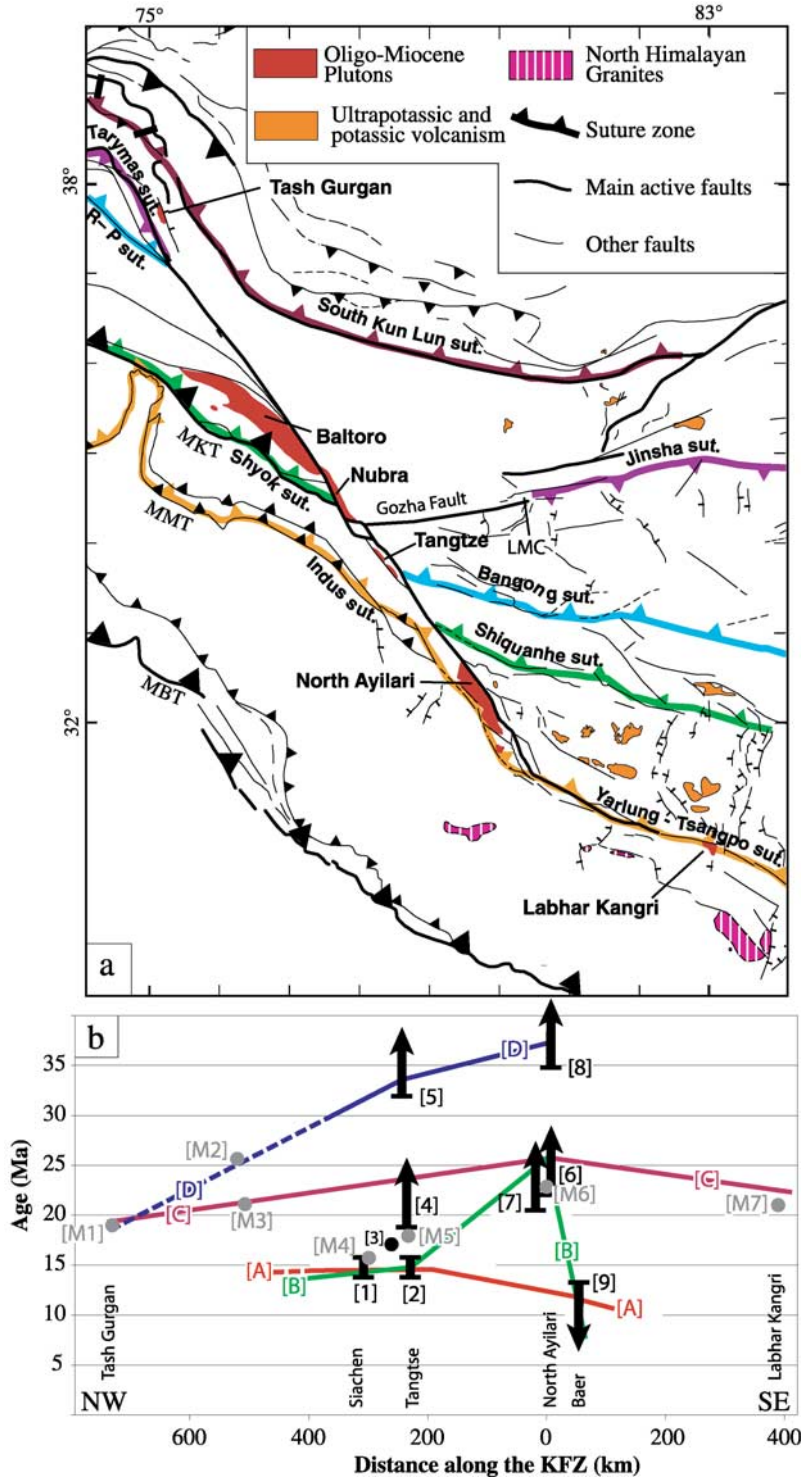
Figure 17

dykes with late ones less deformed and crosscutting earlier transposed ones suggest synkinematic intrusion. (2) The field relationships and microstructures depicted by *Searle and Phillips* [2007, Figure 3] and *Phillips and Searle* [2007] have been interpreted to show that ductile deformation started after 15.6 and stopped at ∼13.7 Ma. However, Ar/Ar thermochronology indicates conditions compatible with ductile deformation (≥300°C) until 10–7 Ma [e.g., *Dunlap et al.*, 1998]. This would imply that right-lateral shear took place during 2 Ma (15.6–13.7 Ma), then stopped during 4 to 7 Ma, before to resume with brittle deformation along the Karakorum fault. Such strange behavior would need to be justified. (3) As in the Ayilari range, pervasive C/S fabrics affect the Tangtse granite [*Searle et al.*, 1998; *Rolland et al.*, 2000]. Such structures are the telltale sign that the granite cooled below solidus during shear [e.g., [*Gapais*, 1989a, 1989b; *Gapais and Barbarin*, 1986]. The fact that strike-slip deformation occurred at and below temperatures close to the granitic solidus (750°C) was indeed mentioned by *Dunlap et al.* [1998, p. 904] and *Weinberg and Searle* [1998, pp. 885 and 890]. (4) The Tangtse granite is intrusive within granulitic (800°C, 5.5 Kb) and amphibolitic (700–750°C, 4–5 Kb) rocks that have been penetratively deformed in a dextral transpressive regime until greenschist conditions were reached [*Rolland et al.*, 2008]. Like the Oligo-Miocene magmatism in the NA range, the intrusion age of the Tangtse granite thus possibly only provides a lower bound to the onset of deformation [*Rolland et al.*, 2008].

[54] If, as seems to be the case, the KFZ affected the Tangtse and Baer area prior to ∼18 and ∼13 Ma respectively, a completely different history of the fault zone, with an early Miocene onset along most of its length, should be proposed ([C] on Figure 17). Because the remaining age constraints only provide a minimum age for initiation of faulting it is not possible to fully reconstruct such history. However, hints are given by the age of Miocene plutonic rocks that appear to emanate from the KFZ (Figure 17, Table 12, and see section 5.5).

[55] A few ages in the NA range and in Tangtse have been interpreted to provide even older constrains for the onset of right-lateral shear: prior to ∼35 and ∼32 Ma respectively ([5] and [8], Table 12, [D] on Figure 17) [*Lacassin et al.*, 2004a; *Rolland et al.*, 2008]. However, in the Ayilari range, there is no structural argument to link the Eocene-Oligocene magmatic event with right-lateral shear (see section 5.2). In Tangtse, the age only rests on the last three heating steps of an amphibole that do not define a

plateau, and correspond to ∼25% of the total gas release. We thus consider this hypothesis ([D] on Figure 17b) as unsubstantiated.

5.5. Miocene Magmatism Along the KFZ

[56] The Baltoro plutonic unit (Figure 1) crystallized in two pulses dated at 25.5 ± 0.3 Ma [*Schärer et al.*, 1990] ([M2] on Figure 17 and Table 12), and 21 ± 0.5 Ma [*Parrish and Tirrul*, 1989; *Schärer et al.*, 1990] ([M3] on Figure 17 and Table 12), at relatively low temperature (750–600°C) [*Searle et al.*, 1992]. The batholith has a sigmoidal shape, with its southern and northern edges striking ∼N110°, 100 km west of the KFZ and progressively bending southeastward to become parallel to the KFZ (N142° strike, Figure 17a). South directed thrusting occurred during granite emplacement along the southern edge of the batholith [*Searle et al.*, 1992]. The eastern border of the batholith is bounded by the KFZ active strand and shows dextral S-C structures [*Searle et al.*, 1998]. Like the Tangtse granite, the Baltoro batholith has been interpreted by *Searle* [1996] and *Searle et al.* [1998] to strictly predate the onset of dextral motion along the KFZ. However, its large-scale sigmoid shape suggests intrusion at least in part synchronous with right-lateral shear along the KFZ, coevally with thrusting along the batholith southern edge and dextral high to medium temperature deformation along its eastern border. In that case, the 25.5 or 21 Ma ages of the granitoid would, as already suggested by *Mahéo et al.* [2004], represent a lower bound for the KFZ timing initiation.

[57] Other evidence for ∼20 Ma magmatism exists along the KFZ trace, while little magmatism of this age is observed far from the fault (Figure 17a) [*Mahéo et al.*, 2002; *Schwab et al.*, 2004, and references therein]. ∼200 km north of the Baltoro pluton, west of Tash Gurgan, an undeformed alkali granite striking parallel to the KFZ (Figure 17a) crystallized at ∼20–18 Ma [*Arnaud*, 1992; *Xie et al.*, 1992], with very rapid cooling from 18 to 11 Ma, according to Ar/Ar data [*Arnaud*, 1992; *Ronghua et al.*, 1996; *Xie et al.*, 1992]. ∼375 km southeast of the Ayilari range, the Labhar Kangri granite, just south of the Zangbo suture branch of the KFZ (Figures 1 and 17a), yields a crystallization age of 21.1 ± 0.3 Ma (section 4.4). The alignment of all these Oligocene-Miocene plutonic units, several of them exhibiting evidence for synkinematic emplacement, suggests that the KFZ acted at that time as a heat source through shear heating and/or as a conduit promoting heat advection for magma ascent. This would imply that the KFZ has been a major discontinuity reaching at least into

Figure 17. Constraints on KFZ initiation timing. (a) Location of Post Eocene magmatism and suture zones in west Tibet. Oligo-Miocene magmatism along the KFZ shown in red. Faults are as on Figure 1. Ultrapotassic and potassic volcanism (orange) mapped from *Arnaud* [1992], *Deng* [1989], *Jiao et al.* [1988], *Liu and Maimaiti* [1989], and *Miller et al.* [1999]. Contours of High and North Himalayan granites (purple with white lines) from *Harrison et al.* [1997, 1999]. Plutonic units along KFZ from this study, *Arnaud* [1992], *Dunlap et al.* [1998], *Jiao et al.* [1988], *Lacassin et al.* [2004a], *Phillips et al.* [2004], *Searle* [1991], and *Searle et al.* [1992, 1998]. Map projection is World Mercator WGS84. LMC: Long Mu Co. (b) Age constraints (Table 12) plotted as a function of distance along the fault. Origin of the x axis corresponding to NA section 3. Oligo-Miocene magmatic events plotted as grey dots, constraints on the onset of the KFZ in black (see Table 12). Four hypotheses (A to D) for the onset and propagation of the KFZ are depicted. See text section 5.4 for details.
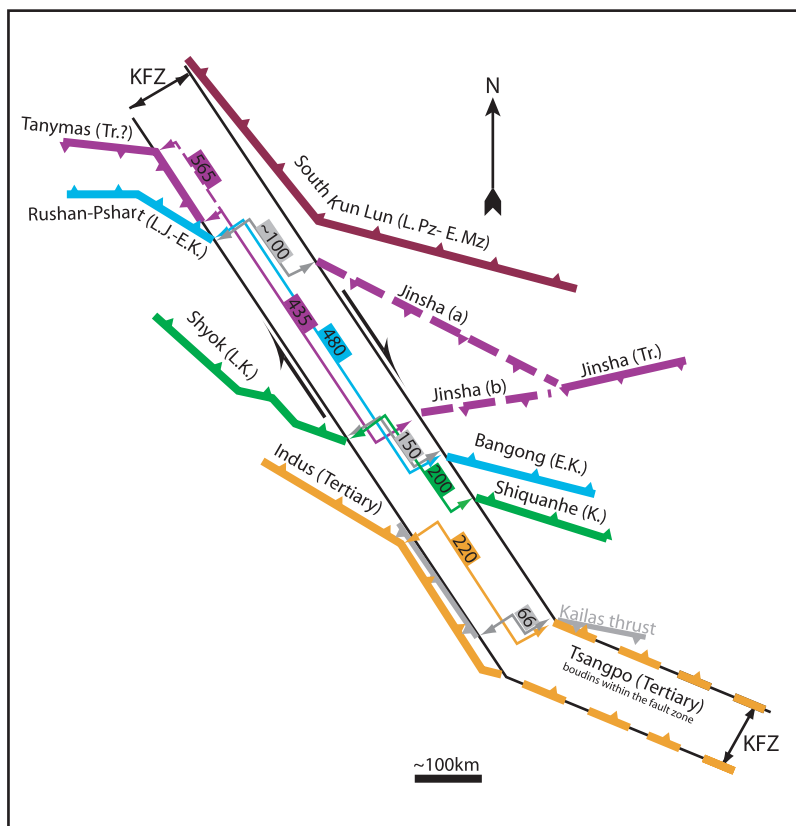
Figure 18. Main suture zones on both sides of KFZ and proposed matches across it. Age of suturing and vergence of each suture are indicated. E, Early; L, Late; Pz, Paleozoic; Mz, Mesozoic; Tr, Triassic; J, Jurassic; K, Cretaceous. North branch of KFZ is artificially widened in order to visualize the offsets (double arrows). Total offset of the Indus-Tzangpo suture for whole Karakorum deformation zone is also indicated, offset on North branch of KFZ being impossible to pin down because KFZ follows the suture. Offset values in kilometers. Preferred matches are in color while gray ones are proposed by *Murphy et al.* [2000] (Kailas thrust and molasses) and *Searle and Phillips* [2007]. See Table 13 and text section 5.6 for details.

the lower crust. The occurrence of mantle-derived magmatic rocks (lamprophyres) along the KFZ north of the Baltoro granite [*Pognante*, 1991; *Searle et al.*, 1992], and in the Tash Gurgan alkaline complex [*Xie et al.*, 1992], further suggests that the KFZ roots at or below the crust-mantle transition. Furthermore, in the Pangong Range, the occurrence of deformed granulites was interpreted as evidence for heat advection along a lithospheric-scale shear zone [*Rolland*, 2002; *Rolland and Pêcher*, 2001; *Rolland et al.*, 2000].

[58] The KFZ shares many characteristics with the ASRR shear zone in Yunnan (SE Asia) which has been interpreted as the Oligo-Miocene continental transform boundary between South China and Indochina [e.g., *Tapponnier et al.*, 1990; *Leloup et al.*, 1995, 2001]. The kinematic link between motion along the ASRR and seafloor spreading in the South China Sea [e.g., *Briais et al.*, 1993; *Harrison et al.*, 1996; *Leloup et al.*, 2001] requires that the shear zone affects the whole lithosphere. In both cases, >1000 km long continental faults absorb large offsets (see section 5.6) during a time period of a couple of tens of Ma long. In both cases, the corresponding shear zone, where exhumed,

is rather narrow (less than 20 km) and shows nearly pure strike-slip deformation coeval with magmatism partly derived from lower crust and mantle partial melting [e.g., *Zhang and Schärer*, 1999]. This leads us to interpret the KFZ as a lithospheric-scale fault shear zone comparable with the Red River, Altyn-Tagh, and North Anatolian fault zones.

5.6. Finite Offsets Across the KFZ, Implication for Long-Term Slip-Rate

[59] The fact that the KFZ is a major boundary that plays an important role in Tibet tectonics is challenged by authors that consider that its long-term slip-rate is low: between 3 and 10 mm/a [e.g., *Phillips and Searle*, 2007]. After a discussion on the most reliable finite offsets, our new timing data will allow us to estimate the KFZ long-term slip rate.

[60] The course of the Indus River is offset ~120 km across the fault north of Shiquanhe (Figure 1) [*Gaudemer et al.*, 1989]. This value only corresponds to a minimum offset on the fault since the incision of the present river course at its present location. Southwest of the active trace of the fault

entrenchment probably occurred during or since rapid exhumation in the North Ayilari range ~16 to 12 Ma ago, thus implying a long-term fault rate ≥8.5 ± 1.5 mm/a [*Valli et al.*, 2007].

[61] *Searle et al.* [1998], *Searle and Phillips* [2004], and *Phillips and Searle* [2007] correlate the Baltoro with the Tangtse granite, which they take to constrain a maximum offset of 120–150 km across the fault near Tangtse. However, because the Tangtse granite is located between two strands of the KFZ, this correlation would only provides the offset on the Southern branch of the fault, hence, a lower bound on the total offset. Furthermore, as the Tangtse granite is possibly synkinematic (see section 5.4), it cannot be used to define a finite offset at all.

[62] A more detailed discussion of offsets across the KFZ is limited by the lack of accurate mapping and poor knowledge of geological structures and of their age. The most reliable markers that can be used to define piercing points along the KFZ at this stage thus appear to be major suture zones. The Indus-Tsangpo suture can be followed continuously from the eastern syntaxis to the Kailas area (Figures 1 and 17). West of the Kailas, the suture zone is smeared into a ~50 km wide zone bounded to the south by the KFZ southern branch [*Lacassin et al.*, 2004a; *Tapponnier et al.*, 1986; *Peltzer and Tapponnier*, 1988]. This branch possibly connects with the Thanglasgo shear zone within the Ladakh batholith (TSZ, Figure 1) [*Weinberg and Dunlap*, 2000], as suggested by right-lateral shear evidences along the Indus suture zone south of Leh [*Stutz and Steck*, 1986; *de Sigoyer et al.*, 2004]. Note that according to cooling histories deduced from Ar/Ar data, right-lateral ductile deformation took place in the TSZ prior to 22 Ma [*Weinberg and Dunlap*, 2000; *de Sigoyer et al.*, 2004], in good accordance with an Oligo-Miocene age for the KFZ. Offset of the Indus suture measured on the south branch of the KFZ reaches ~200 km [*Ratschbacher et al.*, 1994], or ≥220 km [This study] (Figures 17a, 18, and Table 13). A large scale offset ≤400 km is obtained taking into account the whole Karakorum deformation zone [*Lacassin et al.*, 2004a].

[63] Much farther north, the Late Palaeozoic-Early Mesozoic South KunLun suture zone is strongly deflected along the Pamir syntaxis east flank but remains essentially continuous from the western KunLun to the Pamir ranges (Figures 17a and 18) [e.g., *Schwab et al.*, 2004]. Between the Indus and the KunLun three other sutures are found on both sides of the KFZ (Figures 17a and 18). However, their precise location and age has been disputed, leading to conflicting offset estimates across the KFZ (Figure 18 and Table 13).

[64] In the Pamir, the Tanymas suture is probably an equivalent of the Jinsha suture of Tibet [*Schwab et al.*, 2004]. The Jinsha suture and associated rock assemblages in eastern Tibet can be followed westward within central Tibet only to the LongMuCo area [e.g., *Matte et al.*, 1996, Figure 17]. In the absence of detailed mapping, some authors speculate that it extends westward across the Tianshuihai terrane to reach the KFZ North of the K2 [e.g., *Schwab et al.*, 2004; *Yin and Harrison*, 2000] (Jinsha (a) on Figure 18), which would correspond to a ~100 to 130 km offset on the KFZ. The bulk of the large-scale geological evidence [e.g., *Geology Publishing House*, 1998] suggests instead that this suture has been left-laterally offset and dragged along the Gozha fault implying a much larger apparent offset of 435 to 565 km across the KFZ (Jinsha (b) on Figure 18 and Table 13); [*Valli*, 2005].

[65] Farther south in the Pamir, the Late Jurassic–Early Cretaceous Rushan–Pshart suture [*Pashkov and Shvol'man*, 1979; *Shvol'man*, 1980; *Montenat et al.*, 1986; *Burtman and Molnar*, 1993; *Leven*, 1995], is coeval with the Early Cretaceous (100–140 Ma) Bangong suture [*Kapp et al.*, 2003]. The corresponding offset across the KFZ of this characteristic, rather well mapped and well dated feature is ≥400 km [*Lacassin et al.*, 2004a] or ~480 km [This study] (Table 13, Figures 17b and 18). Matching this Late Jurassic suture to the Triassic Jinsha suture on the Tibetan side of the fault [*Searle and Phillips*, 2007] would lead to only ~100 km of offset (Table 13 and Figure 18).

[66] The Late Cretaceous (88–80 Ma) Shyok suture of Pakistan [*Petterson and Windley*, 1985; *Weinberg et al.*, 2000] appears to be a remnant of a back-arc basin that formed between 108 and 92 Ma [*Rolland et al.*, 2000]. The most obvious match of the Shyok suture across the Karakorum fault is the Shiquanhe suture. This yields a minimum offset of 200 to 240 km (Figures 17, 18, and Table 13). In this, we follow *Matte et al.* [1996] who interpret the Shiquanhe mafic and ultramafic rocks as a Late Cretaceous-Paleocene suture continuing eastward across South Tibet to Xainza. Alternatively, *Kapp et al.* [2003] interpreted these rocks as far south travelled klippes from the Bangong suture zone, as did Girardeau et al. [*Girardeau et al.*, 1985] for the Xainza – NamCo ultramafics rocks northwest of Lhasa. In that case the Shyok suture would have no counterpart in southern Tibet. Finally despite their different ages, *Searle and Phillips* [2007] match the Shyok and Bangong sutures across the KFZ, which brings the offset down to ~150 km (Table 1 and Figure 18).

[67] Figure 18 summarizes these diverging views on suture offsets across the KFZ. One view favor small offsets (italic numbers in Table 13) [*Searle and Phillips*, 2007; *Murphy et al.*, 2000]. However, the corresponding interpretations raise the following major problems. (1) The Tanymas suture in the Pamir would have no counterpart in Tibet (Figure 18), while most authors agree that it corresponds both in age and geodynamic significance to the Jinsha suture. (2) Because the Rushan-Pshart and the Jinsha sutures not only have a different age but also a different vergency, it is impossible to match them together. (3) Similarly, matching the Shyok suture with the Bangong suture is just as unlikely. In fact the Shyok back-arc basin (90–110 Ma) was forming at a time when the Bangong realm of the Tethys was in its final stage of closure (100–140 Ma). It seems thus clear that the larger offsets of ~550, ~480, and ≥200 from north to south along the KF are the only ones that make sense (Table 13).

[68] Offsets appear to decrease from NW to SE along the KFZ. This might indicate that the Tertiary KFZ initiated in its NW part and/or has a faster slip rate in that section.

Table 13. Estimates of Suture Zones Offsets Across the KFZ and Corresponding Finite Fault Rates[a]

Suture Zone West of the Karakorum Fault Zone			Match East of the Karakorum Fault			Offset		Finite Fault Rate			
								Oligo-Miocene KKF [C]		Miocene KKF [A]	
Name	Suturing Age	Reference	Name	Suturing Age	Reference	Amount, km	Reference	Age, Ma	Rate, mm/a	Age, Ma	Rate, mm/a
Tanymas	Triassic	*Schwab et al. [2004]*	Jinsha (a)	Triassic	*Schwab et al. [2004]; Yin and Harrison [2000]*	100–130	*Schwab et al. [2004]*	21	5	15	8
Rushan-Pshart	Late Jurassic-Early Cretaceous	*Pashkov and Shvol'man [1979]; Shvol'man [1980]; Montenat et al. [1986]; Burtman and Molnar [1993]; Leven [1995]*	Jinsha (b)	Triassic	*Matte et al. [1996]*	**~435–565**	*Valli [2005]*	21	**21–27**	15	**29–38**
			Jinsha (a)	Triassic	*Schwab et al. [2004]; Yin and Harrison [2000]*	~100	*Searle and Philips [2007]*	22	5	15	7
			Bangong	Early K, 100–140 Ma	*Kapp et al. [2003]*	≥400	*Lacassin et al. [2004a]*	23	≥17	15	27
			Bangong	Early K, 100–140 Ma	*Kapp et al. [2003]*	**480**	This study	23	**21**	15	**32**
Shyok	Late K, 88–80 Ma	*Petterson and Windley [1985]; Weinberg et al. [2000]*	Bangong	Early K, 100–140 Ma	*Kapp et al. [2003]*	~150	*Searle and Philips [2007]*	25	6	14	*11*
			Shiquanhe	Late K?	*Matte et al. [1996]*	280	*Lacassin et al. [2004a]* (whole Karakorum def. zone)	25	11	13	22
Indus	Tertiary		Yarlung-Tzangpo	Tertiary		**≥200 to 240**	This study	25	**≥8 to 10**	13	**≥15 to 19**
						≤400	*Lacassin et al. [2004a]* (whole Karakorum def. zone)	23	17	10	40
						≥220	This study	23	**≥10**	10	**≥22**
						~200	*Ratschbacher et al. [1994]*	23	9	10	20
						66	*Murphy et al. [2000]*	23	3	10	7

[a]Preferred offsets are in bold. Some offsets of *Lacassin et al.* [2004a, 2004b] were measured for the whole ~80 km wide Karakorum deformation zone. In this study, corresponding offsets are measured from piercing points on the trace of the active fault. In any case, uncertainties on measured offsets are difficult to estimate but could reach a few tenths of kilometres. Rates are calculated using initiation ages [A] (italic) and [C] shown in Figure 17b. Preferred rates are bold. See text section 5.6 and Figure 18.

Alternatively, part of the offset in the NW could be inherited from older deformation phases. For example the two largest offsets, between the Triassic (Jinsha / Tanymas) and the Early Cretaceous (Bangong / Rushan-Pshart) sutures, could have accrued along a proto KFZ. Since there is little additional evidence to argue for such a proto KFZ, we have chosen to calculate the slip rates corresponding to the above offsets assuming that all are of Tertiary age (Table 13). Such rates thus correspond to maximum estimates. Dismissing the new age results presented here and assuming that the KFZ is of upper Miocene age (A on Figure 17b), and considering the most improbable smaller offsets, would yield rates between ~6.6 and 11 mm/a (Table 13, italic). With the larger, and more realistic, offsets the rates increase in the 15 to 38 mm/a range (Table 13, bold italic). For an Oligo-Miocene KFZ (C on Figure 17b) the larger offsets yield rates between ≥8 and 27 mm/a (Table 13, bold).

[69] For the southern half of the KFZ, the long-term rates (≥8–10 mm/a, Table 13) are in good agreement with that deduced from the Indus river offset (≥8.5 ± 1.5 mm/a, *Valli et al.*, 2007], with those derived from Quaternary moraines (10.7 ± 0.7 mm/a, *Chevalier et al.*, 2005], as well as with the geodectic rate of *Barnejee and Bürgmann* [2002] (11 ± 4 mm/a). Reasons why other geodetic rates, 3.4 ± 5 mm/a [*Jade et al.*, 2004] and 1 ± 3 mm/a [*Wright et al.*, 2004], appear to be lower than even the lowest geologic rate (6.6 mm/a *Murphy et al.* [2000]) remain to be understood.

5.7. Conclusion

[70] The North Ayilari shear zone was right-lateral prior to ~22.7 Ma ago. This suggests that the Karakorum fault zone is active since at least the Oligo-Miocene. The occurrence of several Oligo-Miocene granites outcropping along the fault zone, some of which showing evidence for synkinematic emplacement, suggest that the KFZ may have played an important role in the creation and /or collection of crustal melts. Considering the most realistic reconstructions of suture zones on both sides of the fault yield integrated rates ≤27 mm/a in the northern section of the fault zone decreasing to ≥8 to 10 mm/a along the Southern section. Dismissing the geochronological results presented in this paper and considering a Miocene age for the onset of the KFZ would significantly increase the fault rates. The KFZ cannot be considered as a small transient fault as it appears to have stayed stable through the Miocene, and have absorbed more than 200 km of displacement for an integrated fault rate on the order of 1 cm/a.

References

Armijo, R., P. Tapponnier, J. L. Mercier, and H. Tonglin (1986), Quaternary extension in southern Tibet: Field observations and tectonic implications, *J. Geophys. Res.*, *91*(14), 13,803–13,872.

Armijo, R., P. Tapponnier, and H. Tonglin (1989), Late Cenozoic right-lateral strike-slip faulting in southern Tibet, *J. Geophys. Res.*, *94*(B3), 2787–2838.

Armijo, R., B. Meyer, A. Hubert, and A. Barka (1999), Westward propagation of the North Anatolian fault into the northern Aegean: Timing and kinematics, *Geology*, *27*, 267–270.

Arnaud, N. (1992), Apports de la thermochronologie ^{40}Ar/^{39}Ar sur feldspath potassique à la connaissance de la tectonique cénozoïque d'Asie, Ph.D. thesis, 155 pp., Univ. de Clermont-Ferrand.

Black, L. P., S. L. Kamo, C. M. Allen, J. N. Aleinikoff, D. W. Davis, R. J. Korsch, and C. Foudoulis (2003), TEMORA 1: A new zircon standard for Phanerozoic U-Pb geochronology, *Chem. Geol.*, *200*, 155–170.

Briais, A., P. Patriat, and P. Tapponnier (1993), Updated Interpretation of Magnetic-Anomalies and Sea-Floor Spreading in the South China Sea: Implications for the tertiary tectonics of South-Asia, *J. Geophys. Res.*, *98*, 6299–6328.

Brunel, M., N. Arnaud, P. Tapponnier, Y. Pan, and Y. Wang (1994), Kongur shan normal fault: Type example of mountain building assisted by extension (karakoram fault, eastern Pamir), *Geology*, *22*, 707–710.

Burtman, V. S., and P. Molnar (1993), Geological and geophysical evidence for deep subduction of continental crust beneath the Pamir, *Spec. Pap. Geol. Soc. Am.*, *281*, 1–76.

Catlos, E. J., C. S. Dubey, T. M. Harrison, and M. A. Edwards (2004), Late Miocene movement within the Himalayan Main Central Thrust shear zone, Sikkim, north–east India, *J. Metamorph. Geol.*, *22*(3), 207–226.

Chappell, B. J., and A. J. R. White (1974), Two contrasting granite types, *Pac. Geol.*, *8*, 173–174.

Chevalier, M.-L., F. J. Ryerson, P. Tapponnier, R. C. Finkel, J. Van Der Woerd, Li Haibing, and Liu Qing (2005), Slip-rate measurements on the Karakorum fault may imply secular variations in fault motion, *Science*, *307*(5708), 411–414.

Clemens, J. D. (2003), S-type granitic magmas-petrogenetic issues, models, and evidence, *Earth Sci. Rev.*, *61*, 1–18.

Compston, W., I. S. Williams, and C. Meyer (1984), U-Pb geochronology of zircons from lunar breccia 73217 using a sensitive high mass-resolution ion microprobe, *J. Geophys. Res.*, *89*, supplement, B525–B534.

Deloule, E. C., M. Chaussidon, B. P. Glass, and C. Koeberl (2001), U-Pb isotopic study of relict zircon inclusions recovered from muong nong-type tektites, *Geochim. Cosmochim. Acta*, *65*(11), 1833–1838.

Deng, W. M. (1989), Volcanism in Tibet, *J. Nat. Res.*, *3*, 205–210.

de Sigoyer, J., S. Guillot, and P. Dick (2004), Exhumation Processes of the high-pressure low-temperature Tso Morari dome in a convergent context (eastern-Ladakh, NW-Himalaya), *Tectonics*, *23*(3), TC3003, doi:10.1029/2002TC001492.

Dunlap, W. J., R. F. Weinberg, and M. P. Searle (1998), Karakoram fault zone rocks cool in two phases, *J. Geol. Soc. London*, *155*, 903–912.

England, P. C., and G. Houseman (1986), Finite strain calculations of continental deformation: 2. Comparison with the India-Asia collision zone, *J. Geophys. Res.*, *91*, 3664–3676.

Gapais, D. (1989a), Les Orthogneiss: Structures, mécanismes de déformation et analyse cinématique, *Mem. Doc. CAESS*, *28*, 1–366.

Gapais, D. (1989b), Shear structures within deformed granites: Mechanical and thermal indications, *Geology*, *17*, 1144–1147.

Gapais, D., and B. Barbarin (1986), Quartz fabric transition in a cooling syntectonic granite (hermitage massif, France), *Tectonophysics*, *125*, 357–370.

Gaudemer, Y., P. Tapponnier, and D. L. Turcotte (1989), River offsets across active strike-slip faults, *Ann. Tecton.*, *3*, 55–76.

Gebauer, D. (1996), A P-T-t-path for an (ultra?-) high-pressure ultramafic/mafic rock-association and its felsic country-rocks based on SHRIMP-dating of magmatic and metamorphic zircon domains; example: Alpe Arami (Central Swiss Alps), *Eos Trans. AGU*, *95*, 307–329.

Geology Publishing House (1998), *Geological Map of Qinhai-Xizang Plateau and Adjacent Areas*, Geol. Publishing House, Beijing.

Gilley, L. D., T. M. Harrison, P. H. Leloup, F. J. Ryerson, O. M. Lovera, and J. H. Wang (2003), Direct dating of left-lateral deformation along the Red River shear zone, China and Vietnam, *J. Geophys. Res.*, *108*(B2), 2127, doi:10.1029/2001JB001726.

Girardeau, J., J. Marcoux, E. Fourcade, J. P. Bassoulet, and T. Youking (1985), Xainxa ultramaphic rocks, central Tibet, China: Tectonic environment and geodynamic significance, *Geology*, *13*, 330–333.

Hanchar, J. M., and R. L. Rudnick (1995), Revealing hidden structures: The application of cathodoluminescence and back-scattered electron imaging to dating zircons from lower crust xenoliths, *Lithos*, *36*, 289–303.

Harrison, T. M., P. H. Leloup, F. J. Ryerson, P. Tapponnier, R. Lacassin, and W. Chen (1996), Diachronous initiation of transtension along the Ailao Shan-Red River shear zone, Yunnan and Vietnam, in *The Tectonic Evolution of Asia*, edited by A. Yin and T. M. Harrison, pp. 208–226, Cambridge Univ. Press, New York.

Harrison, T. M., O. M. Lovera, and M. Grove (1997), New insights into the origin of two contrasting Himalayan granite belts, *Geology*, *25*, 899–902.

Harrison, T. M., M. Grove, K. D. McKeegan, C. D. Coath, O. M. Lovera, and P. Le Fort (1999), Origin and episodic emplacement of the Manaslu intrusive complex, Central Himalaya, *J. Petrol.*, *40*(1), 3–19.

Hoskin, P. W. O., and U. Schaltegger (2003), The Composition of Zircon and Igneous and Metamorphic Petrogenesis, in *ZIRCON*, edited by J. M. Hanchar and P. W. O. Hoskin, *Mineral. Soc. Am.*, *53*, 26–62.

Jiao, S., Y. Zhang, S. Yi, C. Ai, Y. Zhao, Y. Li, H. Wang, J. Xu, J. Hu, and T. Guo (1988), Geological map of Qinhai-Xizang Plateau and adjacent areas, map, Geol. Publishing House, Beijing.

Kapp, P., M. A. Murphy, A. Yin, and T. M. Harrison (2003), Mesozoic and Cenozoic tectonic evolution of the Shiquanhe area of western Tibet, *Tectonics*, *22*(4), 1029, doi:10.1029/2001TC001332.

Lacassin, R., et al. (2004a), Large-scale geometry, offset and kinematic evolution of the Karakorum fault, Tibet, *Earth Planet. Sci. Lett.*, *219*, 255–269.

Lacassin, R., et al. (2004b), Reply to Comment on "Large-scale geometry, offset and kinematic evolution of the Karakorum fault, Tibet", *Earth Planet. Sci. Lett.*, *229*(1–2), 159–163.

Leloup, P. H., R. Lacassin, P. Tapponnier, D. Zhong, X. Liu, L. Zhang, S. Ji, and P. T. Trinh (1995), The Ailao Shan-Red River shear zone (Yunnan, China), Tertiary transform boundary of Indochina, *Tectonophysics*, *251*, 3–84.

Leloup, P. H., Y. Ricard, J. Battaglia, and R. Lacassin (1999), Shear heating in continental strike-slip shear zones: Model and field examples, *Geophys. J. Int.*, *136*, 19–40.

Leloup, P. H., N. Arnaud, R. Lacassin, J. R. Kienast, T. M. Harrison, P. T. Trinh, A. Replumaz, and P. Tapponnier (2001), New constraints on the structure, thermochronology and timing of the Ailao Shan - Red River shear zone, *J. Geophys. Res.*, *106*(B4), 6657–6671.

Leven, E. J. (1995), Permian and Triassic of the Rushan-Pshart zone (Pamir), *Riv. Ital. Paleontol. Stratigr.*, *101*, 3–16.

Liu, J., and Y. Maimaiti (1989), Distribution and ages of Ashikule volcanoes on the West Kunlun mountains, west China, *Bull. Glacial Res.*, *7*, 187–190.

Ludwig, K. R. (1993), PBDAT a computer program for processing Pb-U-Th isotope data, version 1.24, *USGS Open-file report, 88-542*, 1–34.

Ludwig, K. R. (2003), User's manual for isoplot/Ex rev. 3.00, a geochronological toolkit for Microsoft Excel, Berkley Geochronology Center Special Publication No. 4, p. 71.

Mahéo, G., S. Guillot, J. Blichert-Toft, Y. Rolland, and A. Pêcher (2002), A slab breakoff model for the Neogene thermal evolution of South Karakorum and South Tibet, *Earth Planet. Sci. Lett.*, *195*(1–2), 45–58.

Mahéo, G., A. Pêcher, S. Guillot, Y. Rolland, and C. Delacourt (2004), Exhumation of Neogene gneiss dome between two oblique crustal boundaries in south Karakorum (NW, Himalaya, Pakistan), in *Gneiss Domes in Orogeny*, edited by D. L. Whitney, C. Teyssier, and C. S. Siddoway, *Geol. Soc. Am. Spec. Pap.*, *380*, 141–154.

Matte, P., P. Tapponnier, N. Arnaud, L. Bourjot, J. P. Avouac, P. Vidal, Q. Liu, Y. Pan, and Y. Wang (1996), Tectonics of Western Tibet, between the Tarim and the Indus, *Earth Planet. Sci. Lett.*, *142*, 311–330.

Miller, C., R. Schuster, U. Klötzli, W. Frank, and F. Purtscheller (1999), Post-collisional potassic and ultrapotassic magmatism in SW Tibet: Geochemical and Sr-Nd-Pb-O isotopic constraints for mantle source characteristics and petrogenesis, *J. Petrol.*, *40*(9), 1399–1424.

Ministry of Geology of USSR (1989), Geological map of Tadjikistan, USSR republic, and adjacent territories, Map, Vsesojuznoi Geol. Inst. Leningrad, Leningrad.

Montenat, C., J. Girardeau, and J. Marcoux (1986), La ceinture ophiolitique néo-cimmérienne au Tibet, dans les Pamirs et en Afghanistan. Evolution géodynamique comparative, *Sci. Terre, Nancy Mém*, *47*, 229–252.

Moore, D. E., S. Hickman, D. A. Lockner, and P. F. Dobson (2001), Hydrothermal minerals and microstructures in the Silangkitang geothermal field along the Great Sumatran fault zone, Sumatra, Indonesia, *Geol. Soc. Am. Bull.*, *113*(9), 1179–1192.

Murphy, M. A., A. Yin, P. Kapp, T. M. Harrison, L. Ding, and J. Guo (2000), Southward propagation of the Karakoram fault system, Southwest Tibet; timing and magnitude of slip, *Geology (Boulder)*, *28*(5), 451–454.

Murphy, M. A., A. Yin, P. Kapp, T. M. Harrison, C. E. Manning, F. J. Ryerson, L. Ding, and J. Guo (2002), Structural evolution of the Gurla Mandhata detachment system, Southwest Tibet; implications for the eastward extent of the Karakoram fault system, *Geol. Soc. Am. Bull.*, *114*(4), 428–447.

Paquette, J. L., and C. Pin (2001), A new miniaturized extraction chromatography method for precise U-Pb zircon geochronology, *Chem. Geol.*, *176*(1–4), 313–321.

Parrish, R. R. (1987), An improved micro-capsule for zircon dissolution in U-Pb geochronology, *Chem. Geol.*, *66*, 99–102.

Parrish, R. R., and R. Tirrul (1989), U-Pb age of the Baltoro granite, northwest Himalaya, and implications for monazite U-Pb systematics, *Geology*, *17*, 1076–1079.

Pashkov, B. R., and V. A. Shvol'man (1979), Rift margins of Tethys in the Pamirs, *Geotektonika*, *13*, 447–456.

Peltzer, G., and P. Tapponnier (1988), Formation and evolution of strike-slip faults, rifts, and basins during the India-Asia collision: An experimental approach, *J. Geophys. Res.*, *93*, 15,085–15,117.

Petterson, M. G., and B. F. Windley (1985), Rb-Sr Dating of the Kohistan Arc-Batholith in the Trans-Himalaya of North-Pakistan, and Tectonic Implications, *Earth Planet. Sci. Lett.*, *74*, 45–57.

Phillips, R. J., and M. P. Searle (2007), Macrostructural and microstructural architecture of the Karakoram fault: Relationship between magmatism and strike-slip faulting, *Tectonics*, *26*, TC3017, doi:10.1029/2006TC001946.

Phillips, R. J., R. R. Parrish, and M. P. Searle (2004), Age constraints on ductile deformation and long-term slip rates along the Karakoram fault zone, Ladakh, *Earth Planet. Sci. Lett.*, *226*, 305–319.

Pognante, U. (1991), Shoshonitic and ultrapotassic post-collisional dykes from northern Karakorum (Sinkiang, China), *Lithos*, *26*(3–4), 305–316.

Ratschbacher, L., W. Frisch, G. Liu, and C. C. Cheng (1994), Distributed deformation in Southern and Western Tibet as result of the India-Asia collision, *J. Geophys. Res.*, *99*(B10), 19,917–19,945.

Ritts, B. D., and U. Biffi (2000), Magnitude of post-Middle Jurassic (Bajocian) displacement on the Altyn Tagh fault, NW China, *Geol. Soc. Am. Bull.*, *112*, 61–74.

Ritts, B. D., Y. J. Yue, and S. A. Graham (2004), Oligocene-Miocene tectonics and sedimentation along the Altyn Tagh Fault, northern Tibetan Plateau: Analysis of the Xorkol, Subei, and Aksay basins, *J. Geol.*, *112*(2), 207–229.

Rolland, Y. (2002), From intra-oceanic convergence to post-collisional evolution; example of the India-Asia convergence in NW Himalaya, from Cretaceous to present, in *Reconstruction of the Evolution of the Alpine-Himalayan Orogen*, edited by G. Rosenbaum and G. S. Lister, *J. Virtual Explor.*, *8*, 193–216.

Rolland, Y., and A. Pêcher (2001), The Pangong granulites of the Karakoram Fault (Western Tibet): Vertical extrusion within a lithosphere-scale fault?, *C. R. Acad. Sci., Ser. I, II or III*, *332*, 363–370.

Rolland, Y., A. Pecher, and C. Picard (2000), Middle Cretaceous back-arc formation and arc evolution along the Asian margin: The Shyok Suture Zone in northern Ladakh (NW Himalaya), *Tectonophysics*, *325*, 145–173.

Rolland, Y., A. Pêcher, G. Mahéo, and I. M. Villa (2008), Syn-kinematic emplacement of the Pangong metamorphic and magmatic complex along the Karakorum Fault (N Ladakh), *J. Asian Earth Sci.* in press.

Ronghua, X., Z. Yuquan, Y. Xie, P. Vidal, N. O. Arnaud, and Z. Qiaoda (1996), Isotopic geochemistry of plutonic rocks, in *Geological Evolution of the Karakorum and Kunlun Mountains*, edited by P. Yusheng, pp. 137–186, Seismological Press, Beijing.

Rubatto, D., and D. Gebauer (1998), Use of cathodoluminescence for U-Pb zircon dating by ion microprobe (SHRIMP): Some examples from high-pressure rocks of the Western Alps, in *Cathodoluminescence in Geosciences*, edited by M. Pagel et al., pp. 373–400, Springer, Berlin.

Rubatto, D., I. S. Williams, and I. S. Buick (2001), Zircon and monazite response to prograde metamorphism in the Reynolds Range, Central Australia, *Contrib. Mineral. Petrol.*, *140*, 458–468.

Schärer, U. (1984), The effect of initial ^{230}Th disequilibrium on young U-Pb ages: The Makalu case, Himalaya, *Earth Planet. Sci. Lett.*, *67*, 191–204.

Schärer, U., J. Hamet, and C. J. Allègre (1983), The Transhimalaya (Gangdese) plutonism in the Ladhak region: A U-Pb and Rb-Sr study, *Earth Planet. Sci. Lett.*, *67*, 327–339.

Schärer, U., T. M. Harrison, and M. P. Searle (1990), Age, cooling history and origin of post-collisional leucogranites in the Karakoram batholith; A multi-system isotope study N. Pakistan, *J. Geol.*, *98*, 233–251.

Schärer, U., J. Kornprobst, M. O. Beslier, G. Boillot, and J. Girardeau (1995), Gabbro and related rock emplacement crust: U-Pb geochronological and geochemical constraints for the Galicia passive margin (Spain), *Earth Planet. Sci. Lett.*, *130*, 187–200.

Schwab, M., et al. (2004), Assembly of the Pamirs: Age and origin of magmatic belts from the southern Tien Shan to the southern Pamirs and their relation to Tibet, *Tectonics*, *23*, TC4002, doi:10.1029/2003TC001583.

Searle, M. P. (1991), Geology and Tectonics of the Karakoram Mountains, *Map 2538*, John Wiley, Chichester.

Searle, M. P. (1996), Geological evidence against large-scale pre-Holocene offsets along the Karakoram Fault: Implications for the limited extrusion of the Tibetan plateau, *Tectonics*, *15*(1), 171–186.

Searle, M. P., and R. J. Phillips (2004), A comment on "Large-scale geometry, offset, and kinematic evolution of the Karakoram fault, Tibet" by R. Lacassin et al., *Earth Planet. Sci. Lett.*, *229*(1–2), 155–158.

Searle, M. P., and R. J. Phillips (2007), Relationships between right-lateral shear along the Karakorum fault and metamorphism, magmatism, exhumation and uplift: Evidence from the K2-Gasherbrum-Pangong ranges, north Pakistan and Ladakh, *J. Geol. Soc. London*, *164*, 439–450.

Searle, M. P., M. B. Crawford, and A. J. Rex (1992), Field relations, geochemistry, origin and emplacement of the Baltoro granite, central Karakoram, *Trans. R. Soc. Edinburgh, Earth Sci.*, *83*, 519–538.

Searle, M. P., R. F. Weinberg, and W. J. Dunlap (1998), Transpressional tectonics along the Karakoram fault zone, northern Ladakh: Constraints on Tibetan extrusion, in *Continental Transpressional and Transtensional Tectonics*, edited by R. E. Holdsworth, R. A. Strachan, and J. F. Dewey, *Geol. Soc., London, Spec. Pub.*, *135*, 307–326.

Seydoux-Guillaume, A. M., J. L. Paquette, M. Wiedenbeck, J. M. Montel, and W. Heinrich (2002), Experimental resetting of the U-Th-Pb systems in monazite, *Chem. Geol.*, *191*(1–3), 165–181.

Shvol'man, V. A. (2002), A mesozoic ophiolite complex in the Pamirs, *Geotectonics*, *14*(6), 465–470.

Stacey, J. S., and J. D. Kramers (1975), Approximation of terrestrial lead isotope evolution by a two-stage model, *Earth Planet. Sci. Lett.*, *26*, 207–221.

Stern, R. A. (1997), The GSC sensitive high resolution ion microprobe (SHRIMP): Analytical techniques of zircon U-Th-Pb age determinations and perfor-

mance evaluation. Radiogenic age and isotopic studies: Report 10, *Geol. Surv. Can., Curr. Res.*, 1–31.

Stern, R. A., and Y. Amelin (2003), Assessment of errors in SIMS zircon U-Pb geochronology using a natural zircon standard and NIST SRM 610 glass, *Chem. Geol.*, *197*(1–4), 111–142.

Stern, R. A., and N. Sanborn (1998), Monazite U-Pb and Th-Ph geochronology by high-resolution secondary ionmass spectrometry; in Radiogenic age and isotopic studies: Report 11, *Geol. Surv. Can., Curr. Res.*, 1–18.

Stutz, E., and A. Steck (1986), La terminaison occidentale du cristallin du Tso Morari (Haut Himalaya, Laddakh méridional, Inde), *Eclogae Geol. Helv.*, *79*, 253–269.

Tapponnier, P., G. Peltzer, and R. Armijo (1986), On the mechanics of the collision between India and Asia, in *Collision Tectonics*, edited by M. P. Coward and A. C. Ries, *Geol. Soc. London Spec. Pub.*, *19*, 115–157.

Tapponnier, P., R. Lacassin, P. H. Leloup, U. Scharer, D. L. Zhong, H. W. Wu, X. H. Liu, S. C. Ji, L. S. Zhang, and J. Y. Zhong (1990), The Ailao Shan Red River Metamorphic Belt-Tertiary Left-Lateral shear between Indochina and South China, *Nature*, *343*, 431–437.

Tapponnier, P., Xu Zhiqin, F. Roger, B. Meyer, N. Arnaud, G. Wittlinger, and J. Yang (2001), Oblique stepwise rise and growth of the Tibet plateau, *Science*, *294*, 1671–1677.

Tera, F., and G. Wasserburg (1972), U-Th-Pb systematics in three Apollo 14 basalts and the problem of initial Pb in lunar rocks, *Earth Planet. Sci. Lett.*, *14*, 281–304.

Valli, F. (2005), Décrochements lithosphériques dans l'Ouest du plateau du Tibet: Géométrie, âge, décalages cumulés et vitesse de glissement long-terme sur la Faille du Karakorum, Ph.D. thesis, 404 pp., Institut de Physique du Globe de Paris.

Valli, F., N. Arnaud, P. H. Leloup, E. R. Sobel, G. Mahéo, R. Lacassin, S. Guillot, H. Li, P. Tapponnier,

and Z. Xu (2007), Twenty million years of continuous deformation along the Karakorum fault, western Tibet: A thermochronological analysis, *Tectonics*, *26*, TC4004, doi:10.1029/2005TC001913.

Vavra, G., D. Gebauer, R. Schmid, and W. Compston (1996), Multiple zircon growth and recrystallization during polyphase Late Carboniferous to Triassic metamorphism in granulites of the Ivrea Zone (Southern Alps): An ion microprobe (SRHIMP) study, *Contrib. Mineral. Petrol.*, *122*, 337–358.

Weinberg, R. F., and W. J. Dunlap (2000), Growth and deformation of the Ladakh batholith, northwest Himalayas: Implications for timing of continental collision and origin of calc-alkaline batholiths, *J. Geol.*, *108*, 303–320.

Weinberg, R. F., and M. P. Searle (1998), The Pangong Injection Complex, Indian Karakoram: A case of pervasive granite flow through hot viscous crust, *Granitic Magma Dynamics*, J. D. Clemens (convener), *J. Geol. Soc. London*, *155*(5), 883–891.

Weinberg, R. F., W. J. Dunlap, and M. Whitehouse (2000), New field, structural and geochronological data from the Shyok and Nubra valleys, northern Ladakh: Linking Kohistan to Tibet, in *Tectonics of the Nanga Parbat Syntaxis and the Western Himalaya*, edited by M. A. Khan et al., *Geol. Soc. London Spec. Pub.*, *170*, 253–275.

Wiedenbeck, M., P. Alle, F. Corfu, W. L. Griffin, M. Meier, F. Oberli, A. Von Quadt, J. C. Roddick, and W. Spiegel (1995), Three natural zircon standards for U-Th-Pb, Lu-Hf, trace element and REE analyses, *Geostand. Newsl.*, *19*(1), 1–23.

Xie, Y., Y. Zhang, R. Xu, N. Arnaud, and P. Vidal (1992), Characteristics and geological implication of the alkaline complex pluton of Taxkorgan, in *International Symposium on the Karakorum and Kunlun Mountains*, p. 61, Kashi.

Yin, A., and T. M. Harrison (2000), Geologic evolution of the Himalayan-Tibetan orogen, *Annu. Rev. Earth Planet. Sci.*, *28*, 211–280.

Yin, A., T. M. Harrison, M. A. Murphy, M. Grove, S. Nie, F. J. Ryerson, W. X. Feng, and C. Z. Le (1999), Tertiary deformation history of southeastern and southwestern Tibet during the Indo-Asian collision, *Geol. Soc. Am. Bull.*, *111*, 1644–1664.

Yue, Y., B. D. Ritts, and S. A. Graham (2001), Initiation and long-term slip history of the Altyn Tagh fault, *Int. Geol. Rev.*, *43*, 1087–1093.

Zhang, L. S., and U. Scharer (1999), Age and origin of magmatism along the Cenozoic Red River shear belt, China, *Contrib. Mineral. Petrol.*, *134*, 67–85.

—————————

N. Arnaud, Géosciences Montpellier, Université Montpellier 2, CNRS UMR 5243, 34095 Montpellier, France.

E. Deloule, Centre de Recherches Pétrographiques et Géochimiques, CNRS UPR 2300, 54501 Nancy, France.

S. Guillot, Laboratoire de Géologie des Chaînes Alpines, CNRS UMR 5025 Université de Grenoble, 38031 Grenoble, France.

R. Lacassin, H. Li, P. Tapponnier, and F. Valli, Equipe de tectonique, mécanique de la lithosphère, Institut de Physique du Globe de Paris, CNRS-Université Paris 7, 4 place Jussieu, Paris, France.

P. H. Leloup and G. Mahéo, Laboratoire des Sciences de la Terre, Université de Lyon, Ecole Normale Supérieure de Lyon, Université Claude Bernard Lyon 1, CNRS UMR 55570, Bat Géode, 43 Bd du, 69622 Villeurbanne Cedex, France. (herve.leloup@univ-lyonl.fr)

D. Liu and Z. Xu, Laboratory of Continental Dynamics, Institute of Geology, CAGS, 100037 Beijing, China.

J.-L. Paquette, Laboratoire Magmas et Volcans, CNRS UMR 6524- Université Blaise Pascal, 63038 Clermont-Ferrand, France.